Response to the Reviewers

H. Asmuth et al.

March 27, 2020

Dear Reviewers,
First of all, we'd like to thank you for the many detailed and constructive comments on the manuscript. They clearly helped to improve the quality of the paper. Following your suggestions some parts of the paper have been largely restructured. Firstly, parts of the theory on the LBM have been rewritten and extended in order to give a better introduction to people not familiar with the method. Secondly, we extended the code-to-code comparison by an initial study of a turbulent inflow case. As mentioned by Reviewer 1, such a comparison comes with additional challenges in terms of the inflow but we agree that it generally states an improvement to the paper. Lastly, based on the comments of Reviewer 2 as well as remarks of Reviewer 1, we have shortened the investigation of the impact of the third-order limiter, clarified the underlying motivation and corrected our wording in terms of implicit LES. Consequently, also parts of the abstract, introduction and conclusion were adapted with regards to the changes.
Please find below our detailed answers (black) to the comments (blue). Note that line and page numbers referred to in our answers correspond to the new corrected manuscript.

1 Reviewer 1

1.1 General Comments

- The level of detail given is sufficient most of the times, however is lacking in some areas. The introduction to the LBM method needs improvement. Whilst trying to be basic it still assumes a lot of in-depth background knowledge and the notation is inconsistent at times, leading to confusion.
  We have incorporated the more detailed changes suggested in the supplement and rephrased selected parts in all subsections on the LBM. For further details, see our answers to the comments from the supplement.

- Choices of the numerical setup remain unclear and need to be discussed in more detail, especially the sensitivity of their results to those choices.
  Again, we refer to our answers to the supplement comments.

- The authors also should try to avoid subjective statements and rely on quantitative evidence.
  We have added a direct comparison of the two numerical approaches in terms of the L^2-relative error norm providing a more quantitative measure of the observed differences. *See, Figure 6 as well as the in-text discussion on page 14*. The same measures are incorporated in the discussion of the new turbulent inflow case. *See, page 20*.

- Even though the authors mention in the conclusion that "..., the presented work underlines the great potential of wind turbine simulations using the LBM", there is no code-to-code comparison for turbulent inflow cases. They are right to argue that it is difficult to have similar inflow turbulence for both codes (this is also the case when comparing vortex methods with FV solutions), however this should not stop them from conducting at least an initial investigation. Predicting the transition characteristics in uniform inflow, though of academic relevance, might not be the best showcase for the applicability of LBM in engineering wind energy flows. Whilst not adding a turbulent flow case to this paper should not prevent its publication, it diminishes its scientific potential.
  A code-to-code comparison in turbulent inflow is now provided in *Section 5*. As in other studies, the main challenge here related to different downstream evolutions of the imposed turbulence. We have discussed the occurring differences (in an empty domain) without going into too much detail, see *Section 5.1*. After all, a more thorough investigation thereof should be addressed by a more fundamental investigation elsewhere. Still, we agree that the comparison of the wakes in turbulent inflow states a good addition to the paper.

- Additionally, the conclusion is missing some detail on the future flow cases to be investigated and the exact challenges in modelling ABL flows.

We added some elaborations on the upcoming challenges, mostly related to the simulation of wall-modelled boundary layers. *See, page 25.*

1.2 Comments in Supplement

- P. 1, l. 1: The abstract should also reinforce as to why the LB method has such great potential in WE, which ultimately lead to this research. The motivation for conducting this research should be stated at the start of the abstract, ie answer the question: why should readers care?
  We agree. The introductory sentences in the abstract were changed accordingly:
  "The high computational demand of large-eddy simulations (LES) remains the biggest obstacle for a wider applicability of the method in the field of wind energy. Recent progresses of GPU-based (Graphics Processing Unit) lattice Boltzmann frameworks, though, provide significant performance gains alleviating such constraints..."

- P. 1, l. 13: Be more specific and mention actual values for the difference between the two codes in terms of forces, CPU time etc. instead of "good agreement", "difference" "significant speed-up". These statements are subjective.
  We have added an exemplary quantitative statement in the abstract (*P. 1, l 8f.: "The near-wake characteristics in laminar inflow are shown to match closely with, for instance, differences of less than 3% in the wake deficit"*). However, we think that of some of the statements referred to by the reviewer can not be avoided in the abstract. Particularly, as they also have a summarising purpose.

- P. 1, l. 10: What does "generally" mean in this context
  The whole sentence was removed in the rewriting of the abstract.

- P. 4, l. 3: Could be worth mentioning that index notation is used here in three dimensions for describing each node. The grid directions could also be added in some form to Figure 1, without showing necessarily all indices for all nodes.
  Both changed accordingly.

- P. 4, l. 4: For people not familiar with LB methods these lattice specific set of velocities need a little more explanation, as they will otherwise will not understand the difference between lattice velocity c mentioned in Eq(2) and particle velocities. In the end the idea that each particle should end up at another node ie $dx = dt = 1$ actually leads to the statement that all components of e_{ijk} are integers, which is not necessarily obvious, but very important in discretizing the Boltzmann equation. That this also means that multiple speeds exist in D3Q19 and D3Q27 lattice types should be mentioned as this is quite different to classic FV formulations. In this context it could be mentioned that each lattice comes with its own set of weights and velocities, and that weights need to fulfill certain criteria to be suitable to solve NS equations using LB. Showing how the weights matter could be done by showing the actual formulation for f_{ijk}^{eq} or simply stating that they go in there.
  We agree. First of all, we have corrected some inconsistencies in our original manuscript, i.e. a mix of dimensional and non-dimensional units in the same section. The non-dimensionalisation is now solely dealt with in *Section 2.3*. This clearly led to some confusion when it comes to the advection of PDFs. Furthermore, we have added details on the equilibrium (including the weights) as well as the general concept of the two-step collide-and-stream process. *See P. 4-5.*

- P. 4, l. 8: It would be good to add delta x to Figure 1 and explain it. "The cube has side length 2 delta x ...."
  Changed accordingly.

- P. 4, l. 13: Is the summation range important? Is it from -1 to 1?
  Yes, this is arguably often not made very clear in the notation in the LBM literature. We have now expanded the sum explicitly for each coordinate direction (*see Eq. (6)*). Also, we now explicitly mention the space of i, j and k (*see P. 4, l.4*)

- P. 4, l. 14: The order of the moment is the sum of the indices alpha, beta, gamma
  Clearly an important addition. Addition accordingly, *see P. 5, l.1.*

- P. 5, l. 1: Maybe equation?
  Yes, as mentioned earlier, the equation for f^{eq} as well as further explanations were added.

- P. 5, l. 2: Expand here. By only stating the equation its significance remains probably unclear to most people. This is really showing a direct relationship between NS equations and LBE.
  Given the length of a comprehensible elaboration of the Chapman-Enskog expansion (or other similar

approaches), unfortunately, we can not expand on this in great detail and keep on referring to the literature, similarly to the vast majority of applied studies using the LBM. Yet, we have added the crucial aspect that the starting point of the the Chapman-Enskog expansion is a moment expansion of the LBE itself (*P.5, l. 5* which provides a first idea of the general concept and a link to the raw velocity moments introduced before.

- P. 5, l. 4: kinematic
  Changed accordingly.

- P. 5, l. 7: As mentioned further down it might be worthwhile to mention the different steps used in LB. Otherwise pre-/post-collision might be unknown terminology.
  As mentioned above, details thereupon are now provided. *See, Eq. (8) and (9).*

- P. 5, l. 22: Without knowing that LB has a collision and streaming step, this reference might lead to confusion. Maybe another term could be used or the two steps will have to be explained.
  We agree. This should be clarified now due to the aforementioned changes.

- P. 5, l. 25: First time mentioned here in this section, maybe mention already in line 15. Geier ... PDFs, ie.,cumulants. This method is referred to as CLBM. or something like that.
  The abbreviation is now being introduced in the introduction. Also the suggested change to line 15 was incorporated.

- P. 6, l. 6ff.: Until here the connection between lattice and method has not been discussed and should be mentioned earlier.
  We have added the crucial fact that the CLBM is only defined on the D3Q27 lattice as opposed to, e.g. SRT and MRT collision models.

- P. 6, l. 14.: Inflow velocity to the cell? In the end the scaling does depend on each cell otherwise c unequal 1.
  No, "*u_0 is the inflow velocity at the inlet" (see P. 6, l. 29).* More generally, it just refers to a global reference velocity used for the non-dimensionalisation.

- P. 6, l. 29ff.: Is Eq.5 also valid for CLBM and MRT, if so this is not mentioned in previous sections.
  Yes it is. A brief explanation was added in Section 2.2: *"Each moment is then relaxed individually towards a referring equilibrium moment m_{eq}. The individual relaxation rates of the hydrodynamic moments (up to second order) remain physically motivated with the second-order relaxation rate given by Eq. (4)" (See P. 5, l. 19ff).*

- P. 7, l. 23.: Maybe this sentence is sufficient in explaining the adaption by Geier. The following equation does not necessarily add anything to the description if it is not fully explained in detail as Geier did. Currently it is pretty confusing, especially when comparing to Eq8.
  We prefer to keep to explicit formulation of the limiter in the paper. After all, we think that it helps to understand the impact of values chosen later in the comparison in Section 6.

- P. 7, l. 24.: How does the index m translate to those in Eq8? This notation taken from Geier 2017b does not match with the one in Eq8 where omega_{alpha,beta,gamma}
  We have added a clarification that ω_m refers to the relaxation rates of the third-order cumulants and modified our explanation.

- P. 7, l. 25.: What is lambda?
  The limiter λ_m is now explicitly introduced before Eq. (15).

- P. 7, l. 26.: Capital C? In Eq7 c was used. A consistent choice should be made. In section 2.2 capital C represented the scaling coefficients.
  We agree and changed the notation in Eq. (15).

- P. 8, l. 9.: Describe in text
  Description added accordingly.

- P. 8, l. 10.: c is a classic variable for chord, but c is also the lattice speed in this paper. Consider using a different variable name
  The former c (chord) was renamed to c_a to avoid confusion.

- P. 8, l. 14.: distance between the centre and what
  We clarified: *"...and d is the distance from the centre of the blade element to the point in space where the force is applied." (See P.9, l. 3f)*

-

- P. 9, l. 27.: Though it is not crucial to the code-to-code comparison, it would be important to comment on the size of the domain. The boundaries are relatively close for a turbine operating at max Ct. Could a simulation be performed for 4D in the cross-directions to check the influence? NS and LB might be differently impacted by this.
  We initially compared our results to a domain with $5\,D$ cross-section. On the other hand, in our previous study (Asmuth et al., 2019) we used $10\,D$ (however, including grid refinement). Similarly to other studies on blockage (e.g. Sarlak et al., 2016) we did find a small impact on the wake. Yet, notably different behaviour in the two codes could not be observed. Following the Reviewer's suggestion we now added a brief comment on this: *"The resulting blockage ratio amounts to $\beta = 0.022$ and was found to have negligible impact on the code-to-code comparison" (P.8, l.18f.)*

- P. 9, l. 30.: Reference missing or add a figure.
  We added an exemplary figure of the temporal convergence of the TKE in both codes for the laminar and turbulent inflow case with highest resolution, see Fig. 3.

- P. 10, l. 7.: Though implicitly stated, mentioning the grid size ni,nj,nk and total DOF would clearly show that these are not small computations.
  We agree. The numbers are now mentioned in Section 4 (*See P. 11, l.12*).

- P. 10, l. 15.: Explain this choice. From your previous study it seems that there is a large Ma sensitivity at least of the blade forces. This somewhat contradicts the statement in section 2.2 that Ma is a free variable.
  Thanks for pointing this out. The statement in section 2.2 refers to the common pratice in applied studies of the LBM. After all, body forces of such a high magnitude as applied by the ALM seem to be rather special case. Depending on Mach number *and* smearing width the forces can change notably. We now added the folowing comment to clarify this: *"A preceding study has shown that the forces determined by the ALM can be significantly more sensitive to the Mach number than the bulk flow depending on the smearing width (Asmuth et al., 2019). Under consideration of this issue we chose Ma = 0.1 referring to CFL = 0.058 for the CLBM cases. (See P.11, l. 20ff)*

- P. 11, Figure 3.: Make use of markers instead of lines. As the results lie on top of each other as it seems.
  Yes, large parts of the plotted lines overlap. We added markers and some opacity to increase the visibility of the points.

- P. 11, l. 10.: The only reason for choosing a small epsilon is to make the AL behave more like a lifting line. A small epsilon therefore might get you closer to the wake of a full-rotor simulation, if we believe that a lifting line solution is the truth. Choosing a small epsilon only because the spatial resolution allows it, is not really a good motivation.
  In this point we partially disagree. As mentioned by the Reviewer, a smaller epsilon will get the solution closer to the lifting-line solution. Also, more distinct tip-vortices can be resolved if the overall resolution allows for this. As for typical grid resolutions, we therefore think that epsilon should always be chosen as small as the numerical framework allows for (considering numerical stability etc.). In our opinion, not doing so would refer to an introduction of an avoidable inaccuracy. In order to clarify this, we added the following comment: *"Mind, that unnecessarily large smearing widths would imply larger deviations from the underlying lifting line theory and are therefore undesirable" (See P.13, l.3)*

- P. 11, l. 11ff.: Why not use the forces from either method and then prescribing them. Then all differences would originate from the methods and not differences in the forcing.
  This is an interesting idea. Indeed, we employed this approach in a different study in a different context (that is currently under review) by simply prescribing the velocity in the ALM as opposed to sampling it from the flow field. However, for this comparison we deem it important to compare the two set-ups without any modifications. After all, differences in the wake originating from different forces would also be found in later applications of the model and therefore state an inherent characteristic of each numerical set-up.

- P. 12, Figure 4.: It would be nice to show the convergence history of the statistics for both methods. Are they similar? The wiggles in u in the 12D plane for the NS are they hinting at limited averaging? Are these azimuthally averaged profiles?
  The exemplary temporal convergence of the TKE now shown in Fig. 3 gives some insights into this.
  As for the 'wiggles' these are indeed statistically converged characteristics. It seems that this additional inflection typically occurs upstream of the beginning of a larger wake meandering. An instantaneous

impression thereof can also be seen in Fig. 7 in the contour plots. And, no, these plots are not azimuthally averaged.

- P. 14, Figure 6.: What is happening here?
  A brief explanation was given in the caption of the figure. The Ti at this part simply becomes very low. This again seems to be a consequence of the wake being laminar and the low resolution of the referring case.

- P. 15, l.3.: This is appreciated, however adding a few lines to Figure 7 for this case would reinforce your argument, without adding any more words.
  We appreciate this suggestions. Dashed lines of the corresponding cases with the AllOne CLBM were added in the plot along with some modifications of the paragraph discussing it (*See, P. 16, l. 13ff*).

- P. 15, l.3.: Reformulation could help here to ensure the reader understands what is being compared, as it might be unclear. The "Smagorinsky case" also employs the limiter function however lambda is 10^6 and thus the limiter is not active. For the other cases the Smagorinsky model is switched off and instead the implicit nature of the limiter used for damping. In fact what is being compared is LES with ILES. Stating this would make it very obvious. Also what is the motivation for comparing them in the first place? Neither in the introduction nor here is the motivation for this exercise stated, only in the conclusion is the potential of these methods finally mentioned. Are considerable reductions in computational time expected?
  Mostly based on the corrections suggested by Reviewer 2 we have shortened and restructured large parts of this entire case study. The explicit questions raised here by Reviewer 1 should now also be clarified in the new manuscript. Without going into further details here, we therefore refer to the new Section 6.

- P. 25: Not sure Appendix B is needed. Referring to Geier 2017b in the body (as is done) might be sufficient.
  We agree and removed Appendix B.

2 Reviewer 1

2.1 General Comments

- P. 5, l.6.: ν is the kinematic viscosity
  Changed accordingly.

- P. 5, l.6.: Section 2.2: The CLBM is described in Section 1 in physical quantities. The reader unfamiliar with LBM might wonder why in addition a rescaling / normalization would be necessary as sketched in Section 2.2. The answer to this question is that LBMs are generally always implemented in non-dimensional units, meaning $\Delta x^{LB} = \Delta t^{LB} = 1$. This is also the case here as $c_s^{LB} = 1/\sqrt{3}$, which is the non-dimensional lattice speed of sound in LBM. This section should be re-written, the normalization and it purpose expressed more clearly.
  Thanks for pointing out these inconsistencies. After a general revision of Section 2, based on the comments of both reviewers, we have made sure that all formulations in Section 2.1 are consistently given in dimensional form. Furthermore, we have provided extra motivation and clarifications of the non-dimensionalisation in Section 2.3.

- Section 4.2, Table 1: A proper convergence analysis would not evaluate the error norm versus the next finer resolution (which will invariably lead to superconvergence), but employ a reference computation at least 4x finer than the highest resolved computation in order to obtain accurate order of accuracy estimates. However, attempting a convergence analysis for a test case in transition is a somewhat futile effort, as evidenced by Table 1. The CLBM as well as the QUICK scheme should lead to 2nd order accurate results and not 1st order as shown in Table 1. My suggestion is to remove in particular this table.
  We agree that our initial approach might have been misleading. The table was removed in the new manuscript. Our initial motivation though, was to provide a quantitative measure comparing the two numerical approaches. Instead of comparing the convergence of the two approaches, we therefore now provide a direct comparison of the two solutions at each referring grid resolution by means of the L^2-relative-error norm. See, *Figure 6* as well as the in-text discussion on page 14. The same norm is also employed in the new turbulent inflow case to quantify the differences in the resulting velocity profiles. *See, page 20.*

- Section 5 is investigating the influence of a higher-order limiter on the CLBM. The authors apply this parameter instead of the Smagorinsky model for scheme stabilization and imply that this would be implicit

large eddy simulation (ILES). It is not. The idea of ILES is to use a tunable parameter such that inherent scheme dissipation plus tuned dissipation agree with the required subgrid scale dissipation of a particular LES model. The approach obviously requires an exact understanding of dissipation behavior of the numerical scheme in the first place plus an exact understanding of the tunable contribution towards the physical meaningful model limit. Just experimenting with a higher-order limiter only demonstrates the availability of such a tunable parameter, but none of the former. I suggest reducing this section considerably and to eliminate the notion of ILES in most places. This section ultimately only underscores that even in the previous section no fully turbulent wake is developed and even the Smagorinsky model is usually only activated to stabilize the computation. As can be inferred from Fig. 8, no fully turbulent spectrum could be establised. In that sence, not even the Smagorinsky model in combination with CLBM is verified at all by the presented computations.
Thank you for your comment, especially regarding the falsely used term *implicit LES*. Apparently, the term ILES is widely used in the literature in connection with the CLBM despite the lacking understanding of its dissipation behaviour. As there appears to be a lacking documentation of the impact of the limiter, our main motivation was to outline the fact that the choice of λ_m is by no means irrelevant as it largely affects the dissipativity of the scheme. Due to latter we now merely conjecture that it could possibly be used as an ILES approach *if* its behaviour was further understood. Also, following your suggestion we have reduced this section considerably. We now only briefly describe the impact of λ_m in laminar inflow using the contour plot of velocity and Ti. The case study in turbulent inflow in this context was removed entirely. Also, we clarified the motivation for this case study.

Actuator Line Simulations of Wind Turbine Wakes Using the Lattice Boltzmann Method

Henrik Asmuth[1], Hugo Olivares-Espinosa[1], and Stefan Ivanell[1]

[1]Uppsala University, Department of Earth Sciences, Wind Energy Campus Gotland, 621 67 Visby, Sweden

Correspondence: Henrik Asmuth (henrik.asmuth@geo.uu.se)

Abstract. The high computational demand of large-eddy simulations (LES) remains the biggest obstacle for a wider applicability of the method in the field of wind energy. Recent progresses of GPU-based (Graphics Processing Unit) lattice Boltzmann frameworks provide significant performance gains alleviating such constraints. The presented work investigates the potential of ~~large-eddy simulations (LES)~~ LES of wind turbine wakes using the cumulant lattice Boltzmann method (CLBM). The wind turbine is represented by the actuator line model (ALM)~~that is implemented in a GPU-accelerated (Graphics Processing Unit) lattice Boltzmann framework~~. The implementation is validated and discussed by means of a code-to-code comparison to an established finite-volume Navier-Stokes solver. To this end, the ALM is subjected to ~~a uniform laminar~~ both laminar and turbulent inflow while a standard Smagorinsky sub-grid scale model is employed in ~~both~~ the two numerical approaches. The ~~comparison shows a good agreement~~ resulting wake characteristics are discussed in terms of the ~~blade loads and~~ first- and second-order statistics as well spectra of the turbulence kinetic energy. The near-wake ~~characteristics. The main differences~~ characteristics in laminar inflow are shown to match closely with differences of less than 3% in the wake deficit. Larger discrepancies are found in the ~~point of~~ far-wake and relate to differences in the point of the laminar-turbulent transition of the wake~~and the resulting far-wake~~. In line with other studies these differences can be attributed to the different orders of accuracy of the two methods. ~~In a second part the possibilities of implicit LES with the CLBM are investigated using a limiter applied to the third-order cumulants in the scheme 's collision operator. The study shows that the limiter generally ensures numerical stability. Nevertheless, a universal tuning approach for the limiter appears to be required, especially for perturbation-sensitive transitionstudies~~A consistently better agreement is found in turbulent inflow below due to the lower impact of the numerical scheme on the wake transition. In summary, the ~~range of discussed cases outline the general~~ study outlines the feasibility of wind turbine simulations using the CLBM ~~. In addition~~ and further validates the presented set-up in addition to previous studies. Furthermore, it highlights the ~~potential of GPU-accelerated LBM implementations to significantly speed up LES in the field of wind energy .~~ computational potential of GPU-based LBM implementations for wind energy applications. As for the presented cases, near real-time performance was achieved on a single off-the-shelf GPU on a local workstation.

1 Introduction

Large-Eddy Simulations (LES) can provide valuable insights into the aerodynamic interaction of wind turbines. In comparison to modelling approaches of lower fidelity, LES allow for the investigation of aerodynamic effects that are directly associated with the transient nature of highly turbulent flows as found in the atmospheric boundary layer (ABL). Resolving the transient large energy-containing turbulent structures does, however, come at a high computational cost that is far beyond, for instance, Reynolds-averaged approaches (RANS; Mehta et al., 2014). Still, in recent years, LES are increasingly used in engineering-driven contexts. Such are for instance the investigation of fatigue loads in various operating conditions (Storey et al., 2016; Nebenführ and Davidson, 2017; Meng et al., 2018), the effects of turbine curtailment (Nilsson et al., 2015; Fleming et al., 2015; Dilip and Porté-Agel, 2017) or the development and testing of farm-wide optimisation control strategies (Ciri et al., 2017; Munters and Meyers, 2018). With such applications the computational demand of typical case studies increases dramatically when compared to the more fundamental investigations performed in earlier years of LES of the ABL. This increase in computational demand relates both to the size of considered domains as well as the physical time simulated. Examples of the former are simulations of entire offshore wind farms (Churchfield et al., 2012b; Abkar and Porté-Agel, 2013; Nilsson et al., 2015) or large areas of complex orography (Ivanell et al., 2018; Fang et al., 2018). An extreme example of the latter is the work by Abkar et al. (2016) investigating the wakes in a wind farm throughout two diurnal cycles.

Despite the growing capacities of modern high-performance computing (HPC) clusters, computational power remains the biggest bottleneck for such large scale LES applications. Over the last three decades the Lattice Boltzmann Method (LBM) has evolved into a viable alternative to classical CFD approaches with significantly increased computational performance (Malaspinas and Sagaut, 2014; Krüger et al., 2016). This mostly relates to the strict separation of non-linear and non-local terms allowing for excellent parallelisability (Succi, 2015). The LBM therefore also proves to be perfectly suitable for implementations on Graphics Processing Units (GPU). Various authors documented the substantial speed-up factors of such implementations, see, e.g., Schönherr et al. (2011), Obrecht et al. (2013) or Onodera and Idomura (2018), to name a few. Nevertheless, applications of the LBM in the field of ABL flows and wind energy are still rare compared to other fields of fluid dynamics. To date, one of the few prominent applications in the wider field of atmospheric flows are wind comfort assessments and pollution dispersion in urban canopies (e.g., King et al., 2017; Ahmad et al., 2017; Jacob and Sagaut, 2018; Lenz et al., 2019; Merlier et al., 2018, 2019). Other related applications are wind load assessments as presented by Andre et al. (2015), Fragner and Deiterding (2016) or Mohebbi and Rezvani (2018). In the field of wind energy though, the use of the LBM remains rather limited. Deiterding and Wood (2016), Khan (2018) and Zhiqiang et al. (2018) presented simulations of geometrically resolved model-scale wind turbines. Avallone et al. (2018) and van der Velden et al. (2016) on the other hand investigated noise emissions of blade sections. Various fundamental aspects of the LBM in the context of wind energy and particularly wind farm simulations therefore remain untouched, yet crucial for future applications.

One method of special importance for the modelling of wind turbines in LES is the Actuator Line Model (ALM). The ALM as well as other actuator-type models couple a CFD simulation to an extension of the Blade Element Momentum (BEM) method. Using the locally sampled flow velocity, body forces of a blade element are computed using empirically determined lift and drag coefficients of the referring airfoil section. These are then again applied in the domain of the CFD simulation (Sørensen and Shen, 2002; Troldborg et al., 2010). This avoids prohibitively expensive geometrically resolved simulations of the rotor. It is therefore the only feasible way to represent wind turbines in LES on a wind farm scale today (Sanderse et al., 2011; Mehta et al., 2014). Again, fundamental investigations of the ALM in lattice Boltzmann frameworks are still limited, yet crucial for future simulations of entire wind farms. Rullaud et al. (2018) presented a first conceptual study of the ALM in this context. The presented ALM for vertical axes wind turbines was, however, limited to two dimensions, i.e. cross-sectional planes. More recently, Asmuth et al. (2019) presented an initial fundamental investigation of the classical ALM for horizontal axis turbines in a cumulant lattice Boltzmann framework in uniform laminar inflow. Main aspects of the study were the sensitivity of the blade forces of the ALM to the spatial and temporal resolution of the bulk scheme as well as computational performance.

The objective of this paper is to analyse the wake of a single wind turbine simulated with the ALM and the cumulant lattice Boltzmann method (CLBM), a recently developed high-fidelity collision operator, particularly suited for high Reynolds number flows (Geier et al., 2015, 2017b). The ~~presented analysis covers two main aspects. First, the aforementioned validation study of this ALM implementation (Asmuth et al., 2019) shall be extended to the near- and far-wake characteristics. As a reference we consult the solution of a~~ main part of the presented study is based on a code-to-code comparison to a standard finite volume (FV) Navier-Stokes (NS) solver. ~~For the sake of comparability, this code-to-code comparison is performed using a uniform laminar inflow.By doing so, we follow a similar approach as several other code-to-code comparisons, see, for instance, Sarlak et al. (2015a, b) or Martínez-Tossas et al. (2018). The simplicity of the set-up eliminates various uncertainties associated with more complex, yet, possibly more realistic inflow conditions. Also, it becomes more straightforward to analyse the effect of the numerical scheme or turbulence model on the downstream evolution of the wake and particularly the onset of turbulence as recently discussed by Abkar (2018). Secondly, we use~~ Its primary motivation it to extend the aforementioned validation study of this ALM implementation (Asmuth et al., 2019) to the near- and far-wake characteristics. The comparison comprises a laminar and turbulent inflow case, respectively. Furthermore, using the same set-up~~to~~, we briefly evaluate the impact of ~~turbulence modelling on the solution of the cumulant LBM. Here, we compare the use of an explicit sub-grid scale closure, namely a standard Smagorinsky model, with an implicit LES approach realised by means of a~~ a stabilising limiter within the collision operator ~~. Lastly, the explicit and implicit approach are also compared in a turbulent inflow that is prescribed using the method by Mann (1998)~~on the wake characteristics.

To the authors' knowledge, this study constitutes the first application of the CLBM to wind turbine wake simulations. Moreover, application-oriented studies of the utilized parametrised version of this collision operator (as further outlined in Sect. 2) are generally still limited, see Lenz et al. (2019). ~~A~~ Therefore, a further motivation of ~~this study is therefore~~ the study is to show the general potential of wind turbine wake simulations using the LBM and specifically the CLBM. The numerical stability of such simulations using the LBM is not self-evident when using typical, rather coarse grid resolutions.

The remainder of the paper is organised as follows: Sect. 2 provides a brief introduction to the LBM. This includes a description of the underlying numerical concept, characteristics of the cumulant collision model, the use of turbulence models in the CLBM and, lastly, details on the implementation of the ALM. Sect. 3 describes the utilised numerical frameworks and case set-up. In Sect. 4 we present the code-to-code comparison ~~of this CLBM-ALM to the NS reference case. ?? covers the~~ in laminar inflow. A discussion of the ~~effects of turbulence modelling on the wake characteristics. In Sect. 7 we shall briefly touch~~ results in turbulent inflow is given in Sect. 5. The impact of the third-order cumulant limiter is outlined in Sect. 6. Sect. 7 briefly touches upon aspects of computational performance. Lastly, final conclusions and guidelines for future studies are provided in Sect. 8.

2 The Lattice Boltzmann Method

In the following we provide a brief description of the LBM. This comprises a description of the governing equations as well as more specific topics relevant for the presented studies, such as sub-grid scale modelling and the implementation of the ALM. For a more detailed description of the fundamentals the interested reader is referred to the work by Krüger et al. (2016).

2.1 Governing Equations

The LBM solves the kinetic Boltzmann equation, i.e. the transport equation of particle distribution functions (PDF) f in physical and velocity space. PDFs describe the probability to encounter a particle (mass) density of velocity $\boldsymbol{\xi}$ at time t at location $\boldsymbol{x}$. Solving the kinetic Boltzmann equation thus requires a discretisation in both physical and velocity space. Using a finite set of discrete velocities (referred to as velocity lattice, see, Fig. 1) and discretising in space and time one obtains the lattice Boltzmann equation (LBE) in index notation

$$f_{ijk}(t+\Delta t, \boldsymbol{x}+\Delta t\, \boldsymbol{e}_{ijk}) - f_{ijk}(t,\boldsymbol{x}) = \Omega_{ijk}(t,\boldsymbol{x}), \tag{1}$$

where ~~$\boldsymbol{e}_{ijk} = i\boldsymbol{e}_x + j\boldsymbol{e}_y + k\boldsymbol{e}_z$ is the referring~~

$$\boldsymbol{e}_{ijk} = (ic, jc, kc) \tag{2}$$

is the particle velocity vector ~~of each discrete lattice direction~~and $i,j,k \in \{-1,0,1\}$. The ~~collision operator Ω_{ijk} on the right-hand side models the redistribution of f through particle collisions within the control volume. Further details thereupon will be given later. The lattice velocity~~ lattice speed c is chosen such that

$$c = \Delta x/\Delta t = 1 \quad . \tag{3}$$

On uniform Cartesian grids PDFs are therefore inherently advected from their source (black dot in Fig. 1) to the neighboring ~~lattice node~~ nodes during one time step ~~, explaining the simplicity and explicitness of Eq. (1). The necessary scaling of macroscopic quantities to comply with Eq. (3) will be outlined in Sect. 2.3. Generally, macroscopic variables can be simply obtained from the raw velocity moments of the PDFs~~

$$m_{\alpha\beta\gamma} = \sum_{ijk} i^\alpha j^\beta k^\gamma f_{ijk}$$

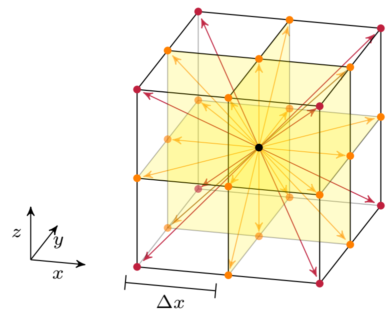

Figure 1. Schematic of three-dimensional velocity lattices. Coordinate-normal planes marked in yellow. ~~The~~ Each vector referring to a discrete velocity $\boldsymbol{e}_{ijk}$ as given in Eq. (1). Velocities of the D3Q19 lattice (Qian et al., 1992) ~~,~~ with 19 discrete ~~velocity~~ directions given by orange vectors. Additional velocity directions considered in the D3Q27 lattice given by red vectors.

~~with α, β and γ denoting the order of the moment in the referring lattice direction. Following dimensional analysis the macroscopic mass density ρ is given by the zeroth-order moment m_{000}. Analogously, the momentum in x, y and z is obtained from the first-order moment in the referring coordinate direction m_{100}, m_{010} and m_{001}, respectively.~~ avoiding any interpolation in the advection. The collision operator Ω_{ijk} on the right-hand side models the redistribution of f through particle collisions within the control volume. Based on kinetic theory the collision process is modelled as a relaxation of particle distribution functions towards an equilibrium. In the classical and most simple collision model, the single-relaxation-time model (SRT), commonly referred to as lattice Bhatnagar-Gross-Kroog (LBGK) model (Bhatnagar et al., 1954), all PDFs are relaxed towards an equilibrium using a single constant relaxation time τ, viz.

$$\Omega_{ijk}(t,\boldsymbol{x}) = -\frac{\Delta t}{\tau}\left(f_{ijk}(t,\boldsymbol{x}) - f^{eq}_{ijk}(t,\boldsymbol{x})\right) \cancel{= -\frac{\Delta t}{\tau} f^{neq}_{ijk}} \cancel{,}. \tag{4}$$

~~with the~~ The equilibrium distribution f^{eq}_{ijk} ~~being~~ is given by the second-order Taylor expansion of the Maxwellian equilibrium

$$f^{eq}_{ijk} = w_{ijk}\,\rho\left(1 + \frac{\boldsymbol{u}\cdot\boldsymbol{e}_{ijk}}{c_s^2} + \frac{(\boldsymbol{u}\cdot\boldsymbol{e}_{ijk})^2}{2\,c_s^4} - \frac{\boldsymbol{u}\cdot\boldsymbol{u}}{2c_s^2}\right) \quad , \tag{5}$$

where c_s is the lattice speed of sound and $\boldsymbol{u}$ and ~~f^{neq}_{ijk} referring to the non-equilibrium part of the distribution functions.A Chapman-Enskog~~ ρ the macroscopic velocity and density, respectively. The weights w_{ijk} are specific to the velocity lattice and ensure mass and momentum conservation of the equilibrium.

Macroscopic quantities can generally be obtained from the raw velocity moments of the PDFs

$$m_{\alpha\beta\gamma} = \sum_{i=-1}^{1}\sum_{j=-1}^{1}\sum_{k=-1}^{1} (ic)^{\alpha}(jc)^{\beta}(kc)^{\gamma} f_{ijk} \tag{6}$$

with α, β and γ denoting the order of the moment in the referring lattice direction and $\alpha+\beta+\gamma$ the total order of the moment. Following from dimensional analysis the macroscopic mass density ρ is given by the zeroth-order moment m_{000}. Analogously, the momentum in x, y and z is obtained from the first-order moment in the referring coordinate direction m_{100}, m_{010} and m_{001}, respectively. The macroscopic velocity and density required for the computation of f^{eq}_{ijk} can thus be obtained locally from the PDFs. Furthermore, starting from a moment expansion of the LBE ~~reveals that~~ itself we can show via a Chapman-Enskog expansion that it recovers the (weakly-compressible) Navier-Stokes equations on the macroscopic level. For the sake of brevity details upon the latter are omitted here. A comprehensive overview can be found in Krüger et al. (2016). Nevertheless, it should be noted that

$$\tau = \frac{1}{\omega} = 3\nu/c^2 + \Delta t/2 \quad , \tag{7}$$

with ν being the ~~shear viscosity~~ kinematic viscosity and ω the relaxation rate (He and Luo, 1997; Dellar, 2001).

In summary, the simplicity of the LBM leads to a straightforward explicit algorithm. Numerically, it is realised by decomposing and rearranging Eqs. (1) and (4) into two separate parts. First becomes the collision step

$$f^{*}_{ijk}(t,\boldsymbol{x}) = \left(1 - \frac{\Delta t}{\tau}\right) f_{ijk}(t,\boldsymbol{x}) + \frac{\Delta t}{\tau} f^{eq}_{ijk}(t,\boldsymbol{x}) \tag{8}$$

where f^{*}_{ijk} is the post-collision distribution function. And, second, is the streaming (or propagation) step

$$f_{ijk}(t+\Delta t, \boldsymbol{x} + \Delta t\, \boldsymbol{e}_{ijk}) = f^{*}_{ijk}(t,\boldsymbol{x}) \tag{9}$$

advecting f^{*}_{ijk} to the neighbouring nodes.

2.2 The Cumulant Collision Model

Due to poor numerical stability of the original LBGK model, various alternative approaches have been presented. These mostly relate to the class of multiple-relaxation-time models (MRT), see for instance Lallemand and Luo (2000) and d'Humières et al. (2002). MRT models transform the pre-collision PDFs f_{ijk} (Eq. (8)) into a velocity moment space. Each moment ~~can then be relaxed~~ is then relaxed individually towards a referring equilibrium moment $m^{eq}_{\alpha\beta\gamma}$ ~~with an individual relaxation time. Subsequently~~. The individual relaxation rates of the hydrodynamic moments (up to second order) remain physically motivated with the second-order relaxation rate given by Eq. (4). Relaxation rates of higher-order moments though can be tuned freely. Subsequently, the moments are transformed back into particle distribution space and advected ~~.~~ following Eq. (9).

Despite significant stability improvements, several fundamental deficiencies of MRT models render the approach unsuitable for high Reynolds number flows as required for studies of wind turbines in the ABL. Referring to the seminal paper by Geier et al. (2015) such are, among others, the lack of a universal formulation for optimal collisions rates, deficiencies stemming from the rather arbitrary choice of moment space, lacking Galilean invariance and the introduction of hyper-viscosities. Deteriorations of the flow field through local instabilities can be the consequence (Gehrke et al., 2017). To remedy the aforementioned deficiencies Geier et al. (2015) suggest a universal formulation based on statistically independent observable quantities (cumulants) of the PDFs, i.e., ~~cumulants~~the CLMB. After performing the two-sided Laplace-transform of the pre-collision

PDFs

$$F(\boldsymbol{\Xi}) = \mathcal{L}\left(f(\boldsymbol{\xi})\right) = \int\limits_{-\infty}^{\infty} f(\boldsymbol{\xi})\, e^{-\boldsymbol{\Xi}\cdot\boldsymbol{\xi}} d\boldsymbol{\xi} \quad , \tag{10}$$

with $\boldsymbol{\Xi} = \{\Xi, \Upsilon, Z\}$ denoting the particle velocity $\boldsymbol{\xi} = \{\xi, \upsilon, \zeta\}$ in wave number space, cumulants $c_{\alpha\beta\gamma}$ can be obtained as

$$c_{\alpha\beta\gamma} = c^{-\alpha-\beta-\gamma} \frac{\partial^{\alpha}\partial^{\beta}\partial^{\gamma}}{\partial\Xi^{\alpha}\partial\Upsilon^{\beta}\partial Z^{\gamma}} \ln\left(F(\Xi,\Upsilon,Z)\right) \quad . \tag{11}$$

Subsequently, cumulants are relaxed towards the referring equilibrium:

$$c^{*}_{\alpha\beta\gamma} = \omega_{\alpha\beta\gamma}\, c^{eq}_{\alpha\beta\gamma} + (1-\omega_{\alpha\beta\gamma})\, c_{\alpha\beta\gamma} \quad . \tag{12}$$

Here, $c^{*}_{\alpha\beta\gamma}$ denotes the post-collision cumulant and $\omega_{\alpha\beta\gamma}$ the referring relaxation rate. As shown by Geier et al. (2015), the statistical independence of cumulants unconditionally eliminates the MRT's deficiencies such as the dependency of Galilean invariance and occurence of hyper-viscosities on the choice of relaxation rates.

A simple and widely adopted choice in the CLBM is to set all relaxation rates of higher-order cumulants to one, commonly reffered to as ALLONE cumulant. In this case, higher-order cumulants are instantly relaxed towards the referring equilibrium. This unconditionally damps all higher-order perturbations providing an inherently stable solution and thereby an extremely robust numerical framework. Numerous studies have shown that the ALLONE CLBM can be readily applied to high Reynolds number flows (see, Geier et al., 2015; Far et al., 2016; Gehrke et al., 2017; Kutscher et al., 2018; Onodera and Idomura, 2018). A further development of the original ALLONE is the parametrised CLBM presented in Geier et al. (2017b). Based on the theory of the so-called *magic parameter* (Ginzburg and Adler, 1994; Ginzburg et al., 2008) the authors derived a parametrisation to optimise the higher-order relaxation rates. The same authors show that the parametrisation increases the convergence of the CLBM in diffusion to fourth order under diffusive scaling (i.e., $\Delta t \propto \Delta x^2$). However, unconditional numerical stability is no longer guaranteed and requires the use of a limiter as outlined in Sect. 2.4.

From a theoretical point of view the parametrised CLBM can arguably be seen as one of the most advanced collision models today, both in terms of accuracy and stability. Nevertheless, the complexity of the collision model ~~as well as the use of a D3Q27 velocity lattice~~ make it more demanding in terms of computational ~~and memory~~ demand compared to SRT and MRT models~~on~~. Furthermore, the CLBM is only defined on the D3Q27 velocity lattice as opposed to SRT and MRT models that typically employ D3Q19 lattices. Consequently, it also requires more memory. In addition to the aforementioned theoretical considerations we therefore provide a pre-study on the suitability of other collision models for this application in Appendix A.

2.3 ~~Scaling and Accuracy of the LBM~~Nondimensionalisation

~~In order to fulfil the aforementioned requirements of the LBE, physical units need to be~~ For the sake of simplicity as well as numerical efficiency and accuracy implementations of the LBM are commonly nondimensionalised. Physical units are therefore rescaled to non-dimensional lattice units (hereafter indexed $(\cdot)^{LB}$)~~, i. e. $c = \Delta x^{LB}/\Delta t^{LB} = 1$. Hence,~~ with $c^{LB} = \Delta x^{LB}/\Delta t^{LB} = 1$. Hence, we can derive scaling factors C for all relevant physical units~~can be derived via non-dimensional quantities~~. As the LBM generally states a weakly compressible method, these are the Reynolds and Mach number Re and Ma, respectively. Within this study we use the cell Reynolds number as $\mathrm{Re}_c = u_0\,\Delta x/\nu$, where u_0 is the inflow velocity at the inlet and Δx grid spacing. The Mach number is consequently given by u_0 and the lattice speed of sound c_s: $\mathrm{Ma} = u_0/c_s$. Starting from the spatial scaling factor we obtain $C_x = \Delta x/\Delta x^{LB} = L_i/n_i$, where L_i is the length of the domain and n_i the number of grid points in the referring spatial dimension. With $c_s^{LB} = c/\sqrt{3}$, the reference velocity on the lattice is given by $\cancel{u_0^{LB} = Ma/\sqrt{3}}$$u_0^{LB} = \mathrm{Ma}/\sqrt{3}$, yielding the velocity scaling factor $\cancel{C_u = \sqrt{3}\,u_0/Ma}$$C_u = \sqrt{3}\,u_0/\mathrm{Ma}$. It follows that the temporal scaling factor is given by $C_t = C_x/C_u$, which implies a physical time step $\Delta t = C_t\,\Delta t^{LB}$ that is inherently proportional to the grid spacing and Mach number. The viscosity in lattice units becomes $\nu^{LB} = \nu C_t/C_x^2$. The order of magnitude of ν^{LB} thus directly depends on the choice of grid resolution and Mach number.

In this study we employ the LBM for an incompressible problem. As in the majority of applications, this implies that compressibility effects are assumed to have negligible effects on the flow physics of interests. The Mach number is thus merely required to be small, yet, does not necessarily have to comply with the physically correct value of the problem. ~~It therefore~~ For incompressible flows it therefore commonly reduces to a somewhat free parameter affecting numerical accuracy in the incompressible limit (Dellar, 2003; Geier et al., 2015, 2017b), computational demand by means of the time step as well as the magnitude of the viscosity on the lattice level.

2.4 Sub-grid Scale Modelling in the LBM

Early on, LES approaches have been used in LBM frameworks (see, e.g., Hou et al., 1996). The most common choice are eddy-viscosity approaches that are simply adopted from NS frameworks and incorporated by adding the eddy-viscosity ν_t to the shear viscosity ν in Eq. (7). Examples thereof range from the standard Smagorinsky model (Hou et al., 1996; Krafczyk et al., 2003) to more advanced models like the wall-adapting local eddy-viscosity model (WALE; Weickert et al., 2010), the shear-improved Smagorinsky model (SISM; Jafari and Mohammad, 2011) as well as dynamic Smagorinsky approaches (Premnath et al., 2009b). Others, on the other hand, suggested LB-specific methods based on the approximate deconvolution of the LBE itself (Sagaut, 2010; Malaspinas and Sagaut, 2011; Nathen et al., 2018).

2.4.1 Implementation of Eddy-viscosity Models

~~The~~ Using a standard constant Smagorinsky model, the eddy-viscosity can be determined locally using the well-known formulation

$$\nu_t = (C_s\,\Delta)^2\bar{S} \quad , \tag{13}$$

where C_s is the Smagorinsky constant, Δ the filter width (here referring to the grid spacing Δx) and $\bar{S}$ the second invariant of the filtered strain rate tensor

$$\bar{S}_{ij} = \frac{1}{2}\left(\frac{\partial \bar{u}_i}{\partial x_j} + \frac{\partial \bar{u}_j}{\partial x_i}\right) \quad \text{, with} \quad \bar{S} = \sqrt{2\,\bar{S}_{ij}\bar{S}_{ij}} \quad . \tag{14}$$

A clear advantage of the LBM over NS approaches in this context is the local availability of the strain rate tensor. Using the second-order moments or cumulants of the local PDFs, respectively, the components of $\bar{S}_{ij}$ can be determined without finite differencing. ~~A detailed description of~~ Further details on the determination of $\bar{S}_{ij}$ in cumulant space ~~is provided in ??~~ can be found in Geier et al. (2015, 2017b). It should be noted~~though~~ , though, that the strain rates in the CLBM and most MRT models are dependent on the total shear viscosity ($\nu_{tot} = \nu + \nu_t$) *and* the bulk viscosity. As opposed to the SRT, where $\bar{S}_{ij}$ is only dependent on the total shear viscosity, it is therefore not possible to explicitly determine ν_t. Hence, the eddy-viscosity $\nu_t(t)$ can be computed either explicitly, using $\nu_t(t-\Delta t)$ or, iteratively. Yu et al. (2005), however, showed that the error associated with the implicitness of ν_t is generally negligible due to the typically small time steps used in the LBM. We shall therefore refrain from implicitly solving for ν_t, in line with similar Smagorinsky approaches in MRT frameworks (Yu et al., 2006; Premnath et al., 2009a).

2.4.2 ~~Implicit LES using~~ Stabilising Limiter in the Cumulant LBM

A crucial characteristic of the CLBM is the model's inherent numerical stability. ~~Even for under-resolved highly turbulent flows~~ As opposed to many other collision model it does not require the stabilising features of explicit turbulence models, even for under-resolved highly turbulent flows. The stabilising characteristic of the original ALLONE cumulant approach appears rather obvious as it unconditionally resets all higher-order cumulants in each time step. The fourth-order accuracy of the parametrised approach, however, relies on the temporal memory of these higher-order cumulants. Therefore, Geier et al. (2017b) suggest the use of a limiter λ_m that is only applied to the relaxation of the third-order cumulants. The relaxation rates ~~ω_m, $m \in \{3,4,5\}$~~ of these cumulants, subsequently referred to as ω_m, are consequently substituted by

$$\omega_\zeta = \omega_m + \cancel{\frac{(1-\omega_m)\,|C_\zeta|}{\rho\lambda_m + |C_\zeta|}}\,\frac{(1-\omega_m)\,|c_m|}{\rho\lambda_m + |c_m|} \quad , \tag{15}$$

where ~~C_ζ~~ $|c_m|$ refers to a the magnitude of the referring third-order cumulant~~(or linear combinations thereof, respectively, as outlined in the original paper)~~. Destabilising accumulation of energy in these cumulants is hereby inhibited as ω_ζ approaches 1 for ~~$\rho\lambda_m \ll |C_\zeta|$~~$\rho\lambda_m \ll |c_m|$. Nonetheless, the order of the error introduced by the limiter lies well below the leading error of the LBM itself. The fourth-order accuracy of the scheme is thus not affected in the asymptotic limit. Alike the ALLONE version, the parametrised CLBM ~~can therefore be applied as implicit LES (ILES)~~therefore does not require the numerically stabilising features of an explicit subgrid-scale model, yet with a higher order of accuracy. In this study we shall therefore focus on the investigation of the parametrised CLBM.

2.5 Implementation of the Actuator Line Model in Lattice Boltzmann Frameworks

The lattice Boltzmann actuator line implementation used in this study closely follows the original description in NS frameworks as presented by Sørensen and Shen (2002). The forces acting on the rotor are determined using the local relative velocity u_{rel} of the referring blade elements along the actuator line. The relative velocity is computed from the sampled velocity in blade-normal (stream-wise) and tangential direction u_n and u_θ, respectively using

$$u_{rel} = \sqrt{u_n^2 + (\Omega r - u_\theta)^2} \quad , \tag{16}$$

where Ω is the rotational velocity of the turbine and r the radial position of the blade element. The local blade force per unit length then reads

$$\boldsymbol{F} = 0.5\,\rho\, u_{rel}^2\, c_a\, (C_L \boldsymbol{e}_L + C_D \boldsymbol{e}_D) \quad , \tag{17}$$

with ~~c being the chord length~~ $\boldsymbol{e}_{L,D}$ being the unit vector in the direction of the lift and drag force, respectively and c_a being the chord length of the referring airfoil section. The lift and drag coefficients C_L and C_D are provided from tabulated airfoil data as functions of the local angle of attack and Reynolds number. The resulting blade forces are subsequently applied across a volume in the flow field by taking the convolution integral of $\boldsymbol{F}$ with a Gaussian regularisation kernel η_ϵ, given by

$$\eta_\epsilon = \frac{1}{\pi^{3/2}\,\epsilon^2}\, e^{-(d/\epsilon)^2} \quad , \tag{18}$$

where ϵ adjusts the width of the regularisation and d is the distance ~~to~~ from the centre of the blade element to the point in space where the force is applied. The resulting force is applied at each grid node by simply adding the referring component of $\Delta t/2\,F$ to the pre-collision first-order cumulants. For the sake of completeness it should be noted that body force formulations generally depend on the collision model. See, for instance, Buick and Greated (2000) and Guo et al. (2008) for a description in SRT and MRT frameworks, respectively.

Differences between ALM implementations in NS and LBM frameworks are obviously small. The latter can be expected given that the link between the model itself and the flow solver is simply made by exchanging information of velocity and body forces. Lastly, it is worth mentioning that the locality of all subroutines of the ALM allows for a perfect parallelisation. The model is therefore efficiently parallelised on the GPU, in line with the general architecture of the utlised LBM solver (see Sect. 3.1) using Nvidia's CUDA toolkit.

3 Numerical Set-up

In light of the code-to-code comparison the simulations in both frameworks were set-up in the most similar manner possible. This refers to the grid, the boundary conditions as well as the implementation of the ALM. Nevertheless, certain differences remain unavoidable due to the inherently different numerical approaches. Further details thereupon as well as the set-up in general will be given in the following.

3.1 The Lattice Boltzmann Solver ELBE

The LBM simulations are performed using the GPU-accelerated Efficient Lattice Boltzmann Environment ELBE[1] (Janßen et al., 2015) mainly developed at Hamburg University of Technology (TUHH). The toolkit comprises various collision models, allows

[1]https://www.tuhh.de/elbe

for free-surface modelling (Janßen et al., 2017) as well as efficient geometry mapping (Mierke et al., 2018). The implementation of the CLBM in ELBE was recently validated by Gehrke et al. (2017, 2020) and Banari et al. (2020).

Symmetry boundary conditions (zero gradient with no penetration) are applied at the lateral boundaries of the domain, referring to a simple-bounce back with reversed tangential components (Krüger et al., 2016). The velocity at the inlet is prescribed using a Bouzidi-type boundary condition (Bouzidi et al., 2001; Lallemand and Luo, 2003), i.e., a simple bounce-back scheme adjusted for the momentum difference due to the inlet velocity. For the outlet we chose a linear extrapolation anti-reflecting boundary condition as described in Geier et al. (2015).

3.2 ELLIPSYS3D

As a NS reference we consult the multi-purpose flow solver ELLIPSYS3D developed at the Technical University of Denmark (DTU) by Michelsen (1994a, b) and Sørensen (1995). The code has been applied to numerous wind power related flow problems and served for several fundamental investigations of the ALM (Sørensen and Shen, 2002; Troldborg, 2008; Troldborg et al., 2010; Sarlak et al., 2015a).

The governing equations are formulated in a collocated finite-volume approach. Diffusive and convective terms are discretised using second-order central differences and a blend of third-order QUICK (10%) and fourth-order central differences (90%), respectively. The blended scheme for the convective term was shown to provide sufficient numerical stability while keeping numerical diffusion to a minimum (Troldborg et al., 2010; Bechmann et al., 2011). The pressure correction is solved using the SIMPLE algorithm. Pressure decoupling is avoided using the Rhie-Chow interpolation.

Symmetry conditions are applied at the lateral boundaries, equivalently to the LB set-up. The outlet boundary condition prescribes a zero velocity gradient.

3.3 Case Set-up

For the evaluation of the ALM we choose one of the most prominent test cases in this context, i.e. the simulation of the NREL 5MW reference turbine (Jonkman et al., 2009)~~subjected to an inflow velocity of~~. The mean inflow velocity in all presented cases is $u_0 = 8\,\mathrm{m\,s^{-1}}$ ~~and operating at~~ while the turbine is operating at an optimal tip-speed ratio of $\lambda = 7.55$. With the viscosity of air $\nu = 1.78 \cdot 10^{-5}\mathrm{m^2\,s^{-1}}$ the Reynolds number with respect to the diameter D amounts to $\mathrm{Re}_D = u_0\,D/\nu = 5.7 \cdot 10^7$ (with $D = 126\mathrm{m}$). The rectangular computational domain spans $6\,D$ in the cross-stream directions and $29\,D$ in the stream-wise direction. The resulting blockage ratio amounts to $\beta = 0.022$ and was found to have negligible impact on the code-to-code comparison. For the sake of comparability, the grid is uniformly spaced in the entire domain. The turbine is located laterally centred $3\,D$ downstream of the inlet. A schematic of the set-up including the definition of coordinates is given in Fig. 2. ~~Based on a prior investigation of the convergence of second-order statistics all~~ All simulations are initially run for ~~4.39~~ $t_0 = 4.39\,T$, with T being one domain flow-through ~~times~~time. Statistics are subsequently gathered over another ~~17.52 domain flow-through times.~~

$17.52\,T$. This choice is based on a prior investigation of the convergence of the second-order statistics. Exemplary plots of the temporal development of the turbulent kinetic energy k are given in Fig. 3.

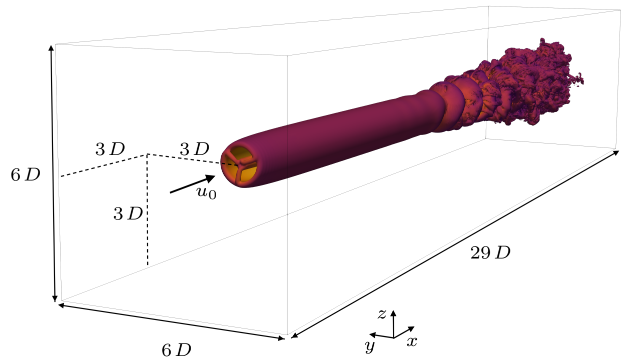

Figure 2. Schematic of the case set-up outlining the dimensions of the computational domain, position of the turbine and definition of coordinates.

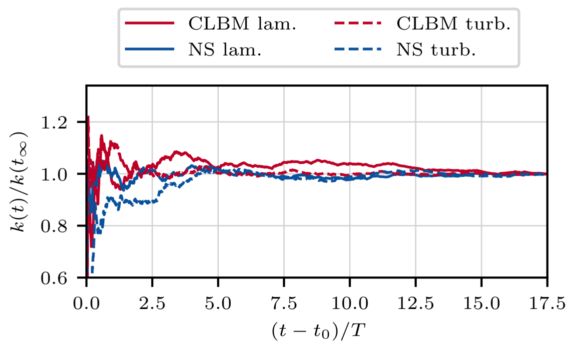

Figure 3. Temporal convergence of the turbulent kinetic energy $k(t)$ at $\boldsymbol{x} = \{24\,D, 0, 0\}$ normalised by the final value $k(t_\infty)$ after $17.52\,T$ averaging. The depicted results refer to the laminar and turbulent inflow cases with a spatial resolution of $\Delta x = D/32$ as discussed in Sects. 4 and 5, respectively.

4 Code-to-code Comparison in Uniform Inflow

As a starting point we compare the results obtained with the CLBM to the NS reference ~~. For this initial investigation a Smagorinsky model is applied in both numerical approaches. The Smagorinsky-constant is set to~~ in uniform laminar inflow. The simplicity of the case eliminates various uncertainties associated with more complex, yet, possibly more realistic inflow conditions. Also, it becomes more straightforward to analyse the effect of the numerical scheme on the downstream evolution of the wake and particularly the onset of turbulence as recently discussed by Abkar (2018).

In both solver we apply the constant Smagorinsky model outlined in Sect. 2.4.1 using a model-constant $C_s = 0.08$, similar to previous studies of the topic (Martínez-Tossas et al., 2018; Deskos et al., 2019). The limiter in the CLBM is set to $\lambda_m = 10^6$ and thus practically switched off. Each model is run with three different grid resolutions $\Delta x = \{D/16, D/24, D/32\}$, referring to 4.4, 14.6 and 34.6 million grid points, respectively. This choice of grid resolutions is below values found in fundamental investigations of, for instance, the evolution of tip vortices (Ivanell et al., 2010; Sarmast et al., 2014). Yet, it lies well within the range commonly found in wind farm simulations using the ALM where higher resolutions might be unfeasible, see, e.g., Porté-Agel et al. (2011), Churchfield et al. (2012a), Andersen et al. (2015) or Foti and Duraisamy (2019). Generally, the tip of the actuator line is required not skip a cell in one timestep Δt in order to ensure a continuous coupling of the ALM with the flow field. In NS-based LES this condition dictates the choice of Δt resulting in a Courant-Friedrichs-Lewy number with respect to u_0 of $\mathrm{CFL} = 0.132$. Referring to Troldborg et al. (2010), the CFL number is thus typically lower than required by the LES to obtain timestep independence. In LBM simulations the timestep is ~~usually~~ dictated by the Mach number as outlined in Sect. 2.3. ~~Choosing $\mathrm{Ma} = 0.1$ we get~~ A preceding study has shown that the forces determined by the ALM can be significantly more sensitive to the Mach number than the bulk flow depending on the smearing width (Asmuth et al., 2019). Under consideration of this issue we chose $\mathrm{Ma} = 0.1$ referring to $\mathrm{CFL} = 0.058$ for the CLBM cases. This is obviously well below the value required by the ALM, yet inevitable due to the numerical method.

As for the ALM, the blades in all cases are discretised by 64 points. The smearing width is set to $0.078125\,D$ referring to $\epsilon/\Delta x = \{1.25, 1.875, 2.5\}$ for the three different resolutions, respectively.

4.1 Blade Loads

Results of the simulations for the time-averaged tangential and normal force components of all cases are given in Fig. 4. BEM (Blade Element Momentum) computations following Hansen (2008) are provided as an additional reference. It becomes obvious that the dependency of the blade forces on the grid resolution is small in both numerical approaches. The same holds for the differences between the CLBM and the NS solution, even though these are found slightly larger than in the former comparison. The deviations from the BEM reference can be related to the influence of the force smearing as well as the lack of a correction model as discussed by Meyer Forsting et al. (2019). Also, despite the relatively low values for $\epsilon/\Delta x$ in the cases with $\Delta x = \{D/16, D/24\}$, no numerical disturbances were caused by ALM in the NS simulations. Note that some authors recommend $\epsilon/\Delta \geq 2$ in order to avoid spurious oscillations (Jha et al., 2013; Martínez-Tossas et al., 2015). Here, instabilities were only found for $\epsilon/\Delta \leq 1$. The choice of ϵ therefore states a compromise~~ensuring~~. On the one hand, it ensures numerical stability for the cases with ~~lowest resolution while keeping it as low as possible~~ the lowest resolution. On the other hand, ϵ is kept reasonably low with respect to the cases with the highest spatial resolution. Mind, that unnecessarily large smearing widths would imply larger deviations from the underlying lifting line theory and are therefore undesirable (Martínez-Tossas and Meneveau, 2019). In summary and in line with other similar code-to-code comparisons (Sarlak, 2014; Sarlak et al., 2015b; Martínez-Tossas et al., 2018) it can be concluded that the agreement in the blade forces is sufficient to facilitate a wake comparison with focus on the behaviour of the bulk scheme.

4.2 Wake Characteristics

Firstly, we compare the time-averaged cross-stream velocity profiles, given in Fig. 5. ~~It can be seen that the~~ Furthermore, Fig. 6 provides a direct comparison of the depicted velocity components of the two numerical approaches ~~agree very well in~~

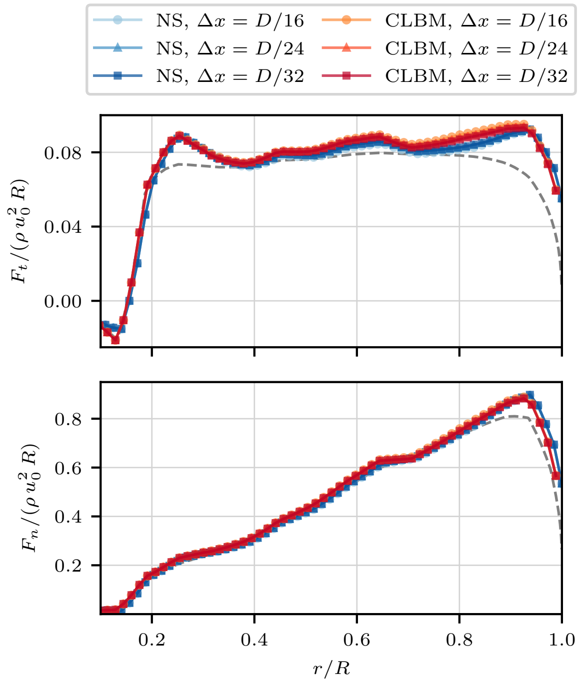

Figure 4. Mean tangential force F_t (left) and normal force F_n (right) along the actuator line. Grey dashed line marking the BEM reference by Hansen (2008).

~~the near-wake of the turbine. The same applies for the observed changes between the grid resolutions. For the stream-wise velocity component we shall quantify this observation~~ at each referring grid resolution by means of the ~~L^1~~ L^2-relative error ~~norm. Specifically, we compute the error $L^1_{ij}(u)$ for the resolved velocity profileof one resolution Δx_i with respect to the next finer resolution Δx_j:~~ along the profile, i.e.

$$L^{\cancel{1}\,2}_{\cancel{ij}}(\cancel{u}\phi) = \cancel{\frac{1}{n_z}\sum_{k=1}^{n_z}\frac{|\overline{u}_i(z(k)) - \overline{u}_j(z(k))|}{|\overline{u}_j(z(k))|}}\sqrt{\frac{\sum_{k=1}^{n_z}\left(\phi_{\mathrm{CLBM}}(z_k) - \phi_{\mathrm{NS}}(z_k)\right)^2}{\sum_{k=1}^{n_z}\phi_{\mathrm{NS}}(z_k)^2}}\quad, \tag{19}$$

where $\phi = \{\bar{u}, \bar{v}\}$ and n_z is the amount of sample points along the profile. ~~Furthermore, we provide the order of grid convergence $p(u(z))$ following the method for non-constant refinement ratios as described in Roache (1998), based on the generalised theory of the Richardson extrapolation. It should, however, be noted that $p(u(z))$ of the presented cases should not be interpreted in the classical sense, i.e., as the asymptotic order of convergence of the numerical methods. This would require solutions within the asymptotic range of convergence. Here, it merely serves as a summarising quantity to facilitate the comparison of the two approaches at different grid resolutions. The mean of $p(u(z))$ along the profile $\langle p(u)\rangle$ as well as $L^1_{ij}(u)$ are given in ??.~~

~~Measures of grid convergence $L^1_{ij}(u)$ and $\langle p(u)\rangle$ of the stream-wise velocity profiles in the near-wake. Index $i, j = 1$ referring to the finest grid, 2 and 3 to the middle and coarse grid, respectively. x 0 D 1 D 3 D 6 D NS 4.44 11.84 19.02 33.47~~

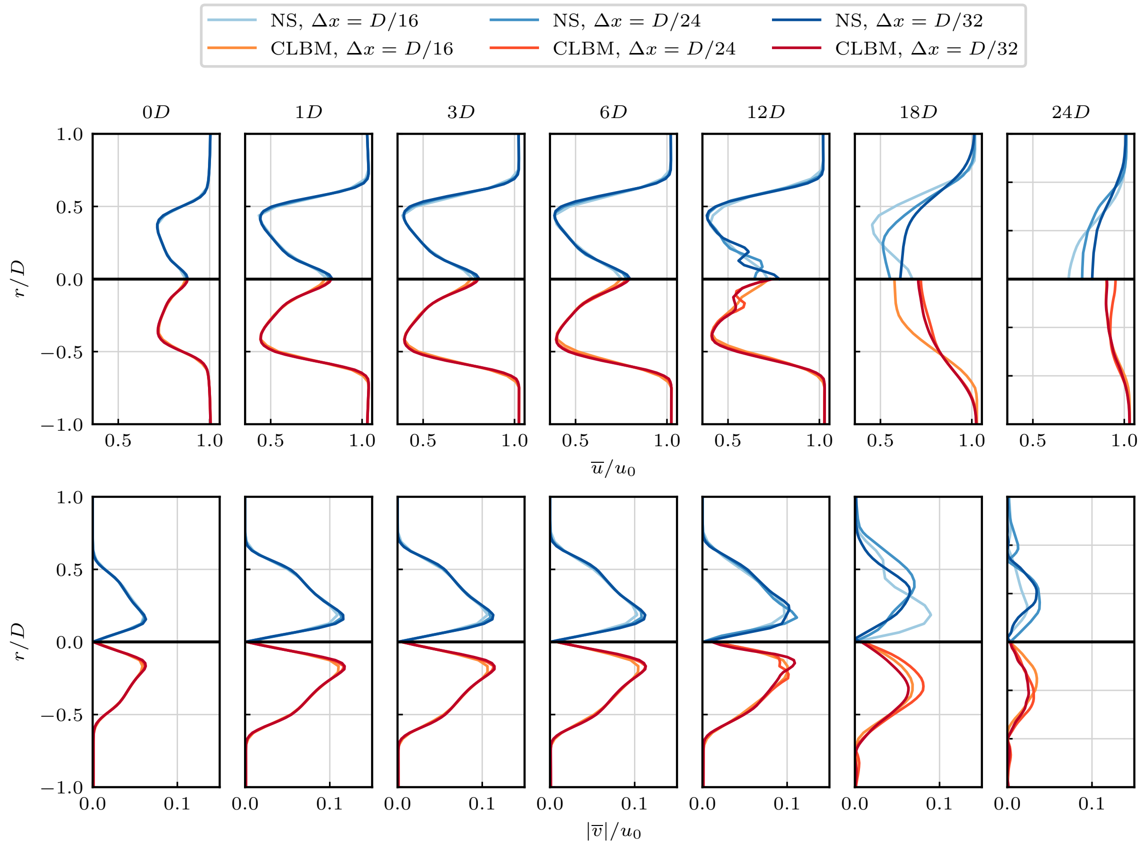

Figure 5. Cross-stream profiles of the mean stream-wise velocity $\overline{u}$ (top) and tangential velocity $\overline{v}$ (bottom) of the CLBM compared to the NS reference cases at different downstream positions.

~~CLBM 3.06 10.26 16.18 23.55 NS 8.73 23.40 41.61 68.37 CLBM 6.21 21.06 32.65 46.80 NS 1.043 1.072 1.026 0.992 CLBM 0.950 0.967 1.254 1.060 It can be seen that the differences between the three spatial resolutions in each numerical approach lie indeed very closely within the same order of magnitude, not only for each refinement step but also at each downstream position.Consequently, the order of convergence is found to be close to one for both approaches at all positions.~~ It can be seen that the two numerical approaches are in good agreement in the near-wake of the turbine. Up until $x = 3\,D$, differences in $\bar{u}$ amount to less than 1% while increasing to $\sim 3\%$ at $x = 9\,D$. The differences in the tangential velocity component $\bar{v}$ are found somewhat higher with $\sim 5\%$ for $x \lesssim 3\,D$ increasing to $\sim 10\%$ at $x = 9\,D$. The latter can be related to the fact we also find higher differences in the tangential than in the normal force component as shown in Fig. 4.

In the near-wake region discussed here, viscous effects usually only play a minor role. This shows, for instance, in a small wake recovery with downstream distance. Also, the rotational velocity does not change significantly. The wake is thus mostly governed by the inviscid flow solution (Troldborg, 2008; Troldborg et al., 2010). Both the NS and the CLBM approach recover

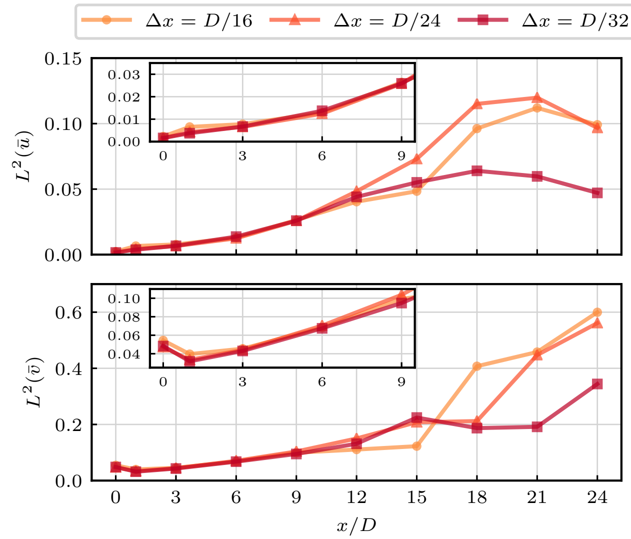

Figure 6. Relative difference (L^2-relative error norm) between the NS and CLBM solution in $\bar{u}$ (top) and $\bar{v}$ (bottom) at each referring spatial resolution along velocity profiles as given in Fig. 5.

the Euler equations at the same order of accuracy. A similar numerical behaviour in this part of the wake should therefore be expected (assuming comparability of all other aspects like boundary conditions and the implementation of the ALM). In light of the motivation for this comparison these results can thus be appreciated.

Further downstream (~~$x > 6\,D$~~$x > 9\,D$) differences between all compared cases increase significantly. Generally, the vortex-sheet of the near-wake starts to meander and eventually breaks down as the wake transitions to a fully turbulent state. An impression thereof is provided in Fig. 7, showing the downstream evolution of the wake in terms of the contour plots of the instantaneous stream-wise velocity. After the onset of turbulence the wake starts to recover more rapidly while the turbulence slowly decays. Differences in the velocity in the far-wake both between the two numerical approaches as well as the referring grid resolutions can therefore be related to different downstream positions of the points of transition.

More quantitatively, the break-down of the wake can be observed by means of a drastic increase in the turbulence intensity Ti as depicted in Fig. 8. It shows that the turbulence intensity in all CLBM cases lies at a similar magnitude in the near-wake. At the same time it is notably higher than in the NS cases at the same downstream position. Downstream of $x = 6\,D$ it can be seen that Ti ~~generally~~ increases faster with downstream distance the higher the spatial resolution. Also, it increases earlier in the CLBM than in the NS solutions. In addition to Fig. 8 this process is illustrated in Fig. 9 by means of the stream-wise evolution of Ti at a radial position of $r/D = 0.625$. It clearly shows the faster increase of Ti at higher spatial resolutions as well as a downstream shift of the build-up in the NS cases.

The mechanism of the transition of wind turbine wakes has been extensively described based on ALM simulations, see, e.g., Sarmast et al. (2014). Fundamental studies thereof do, however, mostly use higher spatial resolutions in order to resolve

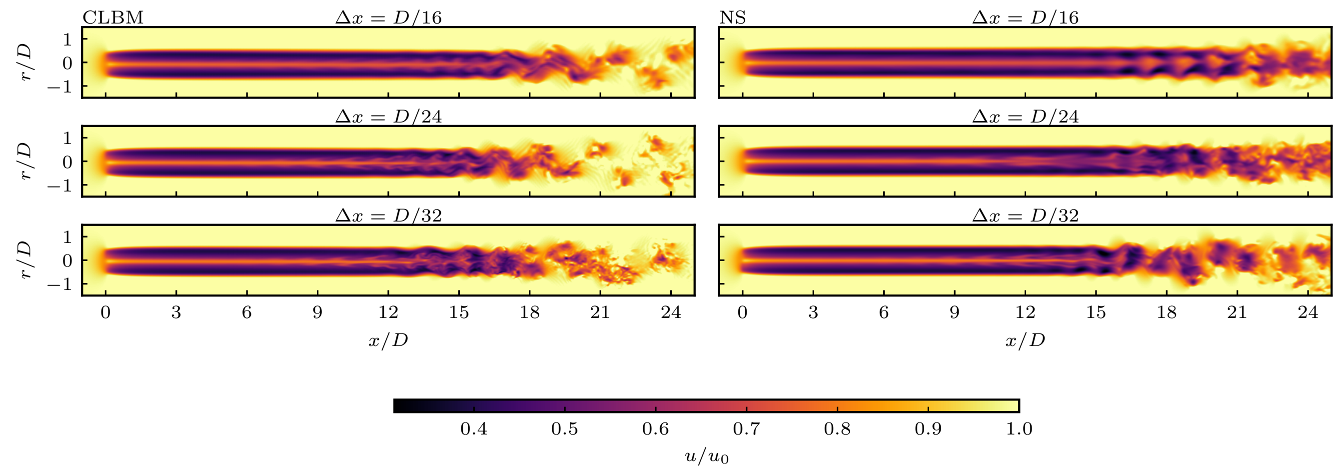

Figure 7. Contour plots of the instantaneous stream-wise velocity u in the central stream-wise plane at different spatial resolutions (top to bottom) with the CLBM (left) and NS (right).

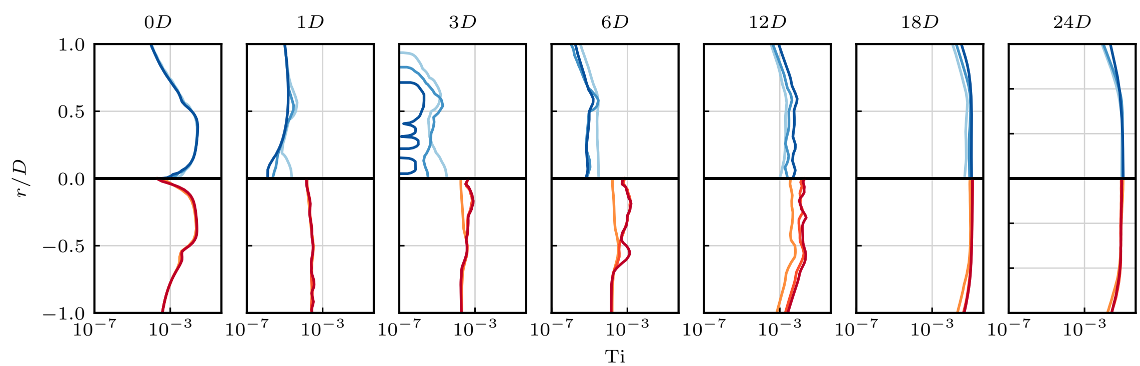

Figure 8. Cross-stream profiles of the turbulence intensity $\mathrm{Ti} = \frac{1}{u_0}\sqrt{\frac{1}{3}\overline{u_i'u_i'}}$ of the CLBM compared to the NS reference cases. Please note the log-scale on the abscissa. Gaps in the line plots (~~e.g.~~ at $x = 3D$) refer to regions of negligible Ti. For legend, see Fig. 5.

distinct tip-vortices. With the resolutions and smearing width used here the wake rather resembles a vortex sheet similarly to actuator disk simulations. To the authors' knowledge only Martínez-Tossas et al. (2018) briefly described the transition process of wakes of such low-resolution ALM. In their discussion of a similar code-to-code comparison the authors argue that small perturbations at high wave numbers eventually trigger the transition of the wake. Schemes with lower numerical diffusivity (pseudo-spectral approaches in that study) generally dampen those perturbations less than more diffusive lower-order schemes (referring to second-order collocated finite-volume discretisations, equivalently to the NS reference used here) and thus show a faster growth of turbulence. The same interpretation can indeed be applied to the results shown here. As described in Sect. 2, the parametrisation of the relaxation rates results in a scheme with fourth-order accuracy in diffusion as opposed to the second-

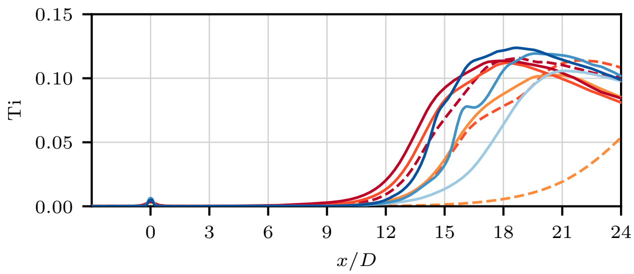

Figure 9. Stream-wise evolution of the turbulence intensity Ti at $r/D = 0.625$ in the CLBM and NS cases. For legend, see ~~Fig. 5~~Fig. 4. Additional dashed lines refer to AllOne CLBM results. These briefly illustrate the impact of the increased order of accuracy when using the parametrised relaxation rates of the CLBM on the wake transition.

order accuracy of the NS finite-volume scheme. At this point we shall briefly comment on the second-order accurate AllOne CLBM mentioned earlier (Sect. 2). In fact, using this version of the CLBM shifts the transition further downstream when compared to the ~~transition behaviour at all resolutions was found to be more similar to the NS solution~~parametrised CLBM, see Fig. 9. This generally corroborates the aforementioned discussion on the effect of the numerical diffusivity. As for this case, the scheme even appears to be more diffusive than the NS solution. Mind, however, that the diffusivity of the AllOne CLBM also strongly depends on the Mach number (as opposed the parametrised approach). Nevertheless, a further analysis of the AllOne CLBM is not the focus of this study and omitted here for the sake of brevity.

As a last aspect of the code-to-code comparison we analyse the one-point turbulence kinetic energy spectra. The spectra shown in Fig. 10 represent the average of sixteen points in the referring cross-sectional plane at a radial position of $r/D = 0.625$. For additional smoothing the Welch method was applied at each point with non-overlapping time intervals of a fifteenth of the overall sampling period.

The energy content in the near-wake ($x = 1\,D$) is expectedly small when compared to the far wake where the vortex sheet has broken down in most of the shown cases. The energy level across most frequencies is indeed low enough to be related to numerical noise making a further interpretation obsolete. The only distinct feature at $x = 1\,D$ are notable peaks at the blade-passing frequency f_B and its higher harmonics. These are found in all presented cases, yet generally slightly smaller in the NS solutions. This signature at f_B was recently described by Nathan et al. (2018) but using twice as many grid points per diameter when compared to the highest resolution shown here. It can thus be appreciated that this transient feature of the ALM remains traceable down to resolutions of $\Delta x = D/16$.

At $x = 12\,D$ a pre-transition wake meandering can be seen. The occurrence of this feature is not as confined to a single frequency as the aforementioned blade-passing frequency. Yet, an increased energy level in a frequency band around $f_m \approx 0.025\mathrm{Hz}$ (and its higher harmonics) can be observed in all cases. It was illustrated in Fig. 7 that the meandering starts to occur at different positions downstream depending on the resolution and numerical approach. It then steadily increases until the wake becomes fully turbulent. The amplitudes at f_m therefore differs depending on how far upstream the meandering started to build

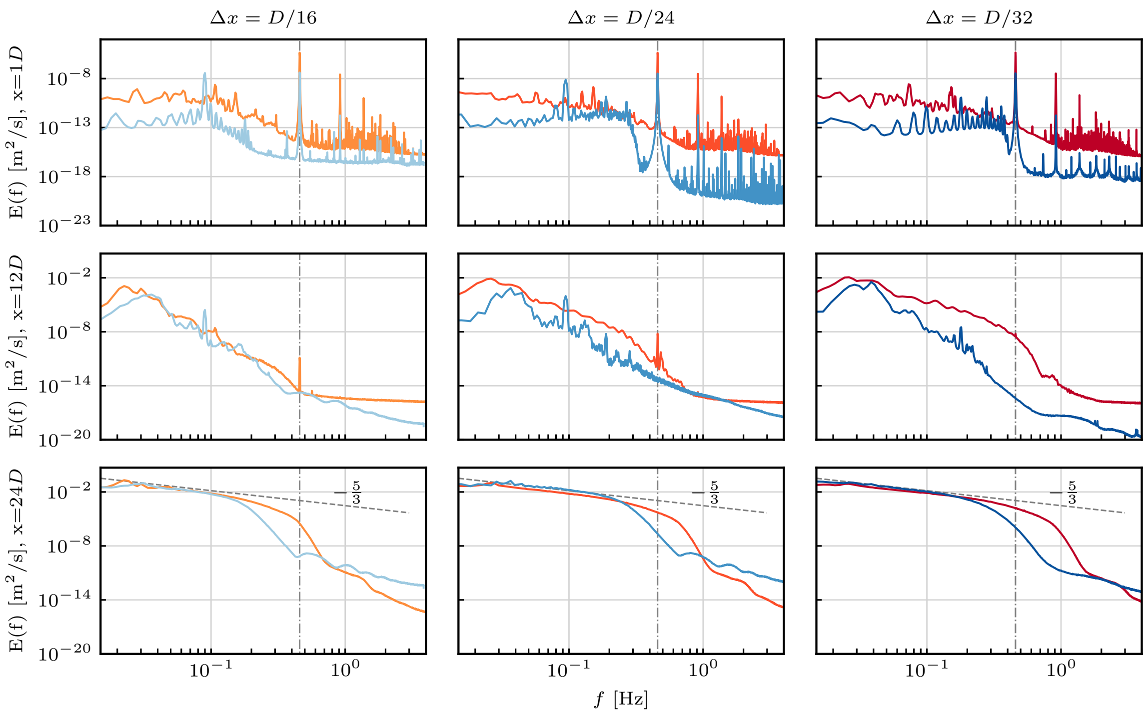

Figure 10. One-point turbulent kinetic energy spectra in the near- ($x = 1\,D$, top) and far-wake ($x = 12\,D$, middle; $x = 24\,D$, bottom) at increasing spatial resolution from left to right. Vertical dashed-dotted line marking the blade-passing frequency $f_B = (3u_0\lambda)/(\pi D) = 0.458$Hz. Mind the change of scale on the y-axis between the first and second row of subplots. For legend, see Fig. 5.

up. Also, it again shows that the meandering and subsequent transition occurs earlier in the CLBM cases. Additionally, the signature of the blade passage is still visible in the lower-resolution CLBM cases. This is not the case for the NS reference, despite the smaller meandering at this downstream position. In line with the observations made earlier, this aspect might relate to a higher numerical dissipation of the NS scheme.

Further downstream at $x = 24\,D$ the wake is fully turbulent in all CLBM cases, characterised by a sub-intertial range with typical -5/3-slope. This is also the case for the NS solution with $\Delta x = D/32$. Here, however, the meandering is still more visible due to the later start of the transition of the wake. Also, when comparing both approaches at the highest spatial resolution (bottom right in Fig. 7) it shows that the sub-inertial range of the CLBM approach reaches to higher frequencies. In accordance with that, it appears that the CLBM does indeed resolve smaller turbulent structures, as shown in the contour plot of the Q-criterion (Fig. 11).

4.3 ~~Discussion~~

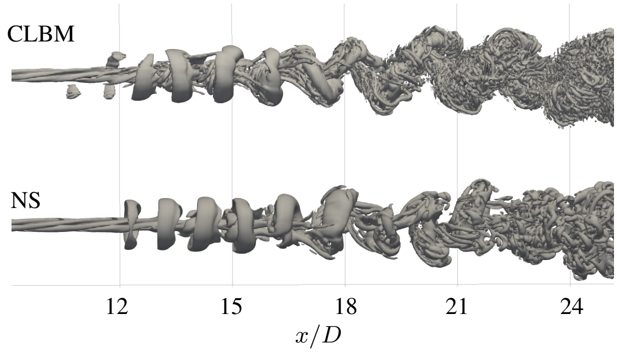

Figure 11. Rendering of the instantaneous contours of the Q-criterion ($Q = 0.0005$) in the far-wake with the CLBM and NS with $\Delta x = D/32$.

~~The results presented here generally show that the CLBM provides a numerical framework the ALM can be readily applied in . In addition to our previous study (Asmuth et al., 2019) this further validates the LBM-ALM implementation discussed here. Also, it extents previous demonstrations of the robustness of the ALM with respect to the numerical approach to a new model, i. e. the CLBM. In line with the code-to-code comparisons referred to earlier (Sarlak, 2014; Sarlak et al., 2015a, 2016; Martínez-Tossas et al., we can highlight three main aspects~~

5 Code-to-code Comparison in Turbulent Inflow

Laminar inflow cases allow for a good comparison of fundamental numerical aspects as discussed in Sect. 4. Nevertheless, the case itself remains rather academic as atmospheric inflows are mostly turbulent. Furthermore, Sect. 4 has shown that a direct comparison of the far-wake can be difficult due to the different downstream positions of the laminar-to-turbulent transition of the wake. A turbulent inflow generally accelerates the transition while reducing the dependency of the point of transition on the numerical diffusivity of the scheme. A complementing comparison in turbulent inflow will therefore be presented in the following. For the sake of brevity we limit the discussion to cases with the highest spatial resolution $\Delta x = D/32$. Apart from the introduction of turbulence at the inlet both numerical set-ups remain unchanged. Also note, that the mean resulting blade loads exhibit no notable difference towards the laminar inflow case. An additional discussion to Sect. 4.1 is therefore omitted.

5.1 Synthetic Turbulence Generation at the Inlet

At the inlet we prescribe homogeneous isotropic turbulence (HIT) based on the von Kármán energy spectrum. The three-dimensional field of velocity fluctuations is generated based on the method by Mann (1998) using the open-source code TuGen by Gilling (2009). As we are only interested in HIT the model's shear parameter Γ is set to zero. The length scale of the spectral velocity tensor is chosen as $L = 40\text{m} = 0.317\,D$. The mean turbulence intensity is scaled via the coefficient $\alpha\epsilon^{2/3} = 0.01$. The resulting Ti of the turbulence field measures $\text{Ti} = 0.028$. The length of the turbulence field in the stream-wise direction measures

24576m. Following Taylor's frozen turbulence hypothesis the field is advected with u_0. The turbulence field is consequently recycled after 6.72 domain flow-through times. The lateral dimensions of the field are set to 1536m (referring to 12.19 D). Since we only use a cross-section of ~~the comparison:~~ $6\,D \times 6\,D$ we ensure zero correlation of the velocity fluctuations between the lateral boundaries of the domain. The spatial resolution of the field is 8192 grid points in the stream-wise direction and 64 grid points in the lateral directions. In both numerical approaches the velocity fluctuation is superimposed with the mean inflow velocity u_0 and applied at the inlet.

Fig. 12 compares the stream-wise evolution of the turbulence intensity at hub-height without ALM. At the inlet we find

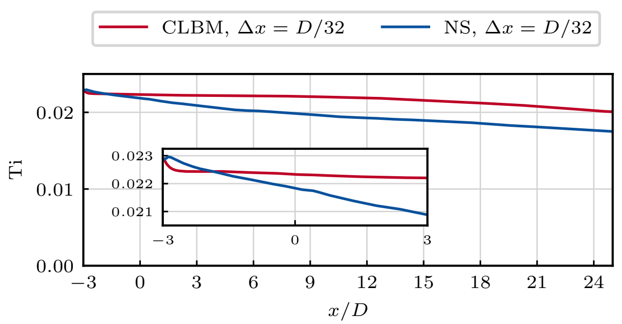

Figure 12. Stream-wise evolution of the turbulence intensity Ti without ALM. Each data point Ti(x) refers to the spatial mean of 64 points in the cross-stream direction z with $-D \leq z \leq D$.

a turbulence intensity of 2.3% in both approaches which is slightly lower than the one of the synthetic turbulence field. Such discrepancies have been discussed earlier and are commonly counteracted by scaling a given turbulence field if a desired turbulence intensity is to be matched (see, e.g. Olivares-Espinosa et al., 2018; van der Laan et al., 2019). Some possible explanations of this issue are given by Gilling and Sørensen (2011). Among others, they argue that the discrete representation of the otherwise continuous turbulence field can lead to noticeable discontinuities when being differentiated with low-order schemes. Directly after the inlet the NS solution shows a small increase in Ti followed by a continuous decay throughout the entire domain. The turbulence intensity in the CLBM solution initially drops behind the inlet. However, the subsequent decay up until $x = 12\,D$ is lower than in the NS solution. Only at the far end of the domain the decay rates of the two approaches seem to align. As a result, the turbulence intensity at the turbine position differs by $\Delta\mathrm{Ti} = 0.0005$ while the maximum difference further downstream amounts to $\Delta\mathrm{Ti} = 0.0027$. A detailed analysis of the rather fundamental aspects related to these discrepancies goes beyond the scope of this paper. After all, the observed differences remain small enough not to be significant when compared to the turbulence related to the wake flow, as shown later.

Fig. 13 depicts the spectra of the turbulent kinetic energy at the turbine position. Chiefly, it shows that the CLBM exhibits a sub-inertial range extending to higher frequencies than the NS solution, similarly to the far-wake turbulence found in laminar inflow (see Fig. 10).

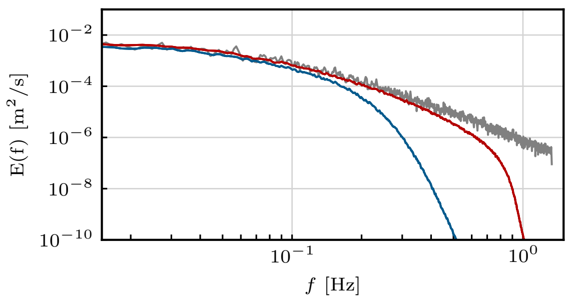

Figure 13. One-point turbulent kinetic energy spectra at the turbine position ($x = 0\,D$) without ALM. The spectrum of the synthetic inlet turbulence is given in grey. For legend, see Fig. 12.

5.2 Wake Characteristics

Analogously to Sect. 4, we firstly compare the cross-stream profiles of the mean velocity in Fig. 14. In the stream-wise velocity component $\bar{u}$ we find an excellent agreement ~~in the~~ of the two solutions. When compared to the laminar cases discussed before this not only applies to the near-wake ~~, differences in~~ but the entire domain. The difference in $\bar{u}$ between the cross-stream profiles of the ~~point of transition depending on the order of accuracy in diffusion and , again, a good~~ two approaches for $x \lesssim 9\,D$ amounts to less than 1% in terms of the L^2-relative error norm. The maximum discrepancy measures 1.6% and is found at $x = 24\,D$. Mind, that the laminar inflow cases only exhibited similar agreements in the near-wake.

Profiles of the turbulence intensity are shown in Fig. 15. Similarly to the velocity, differences between the CLBM and NS solutions are small. Most importantly, it can be observed that the transition of the wake is triggered at very similar downstream positions. This also explains the significantly better agreement in the ~~far-wake after the~~ velocity. After all, most differences observed in laminar inflow are related to the different downstream positions of the laminar-to-turbulent transition.

6 ~~Comparison of Implicit and Explicit Sub-grid Scale Modelling in the Cumulant LBM~~

~~Previous studies have shown that the additional damping introduced by sub-grid scale models can have a significant impact on the point of transition of wind turbine wakes in uniform inflow. See, for instance, the code-to-code comparison studies mentioned above or the recent works by Abkar (2018) or Deskos et al. (2019). The near-wake characteristics as well as the blade loads, on the other hand, are usually not much affected. Conversely, the~~ In the case discussed here the transition is dominated by instabilities introduced by the ambient turbulence. As opposed to the transition in laminar inflow, the impact of the dissipative characteristics of the numerical scheme here appears to be subordinate, if not negligible. Without imposed turbulence, perturbations triggering the transition grow within the wake itself starting from infinitesimal magnitudes as outlined in Sect. 4. Hence, the transition mainly depends on the growth of such perturbations and eventually the point where they reach a critical magnitude. Consequently, the transition is increasingly delayed the higher this growth is damped by the numerical

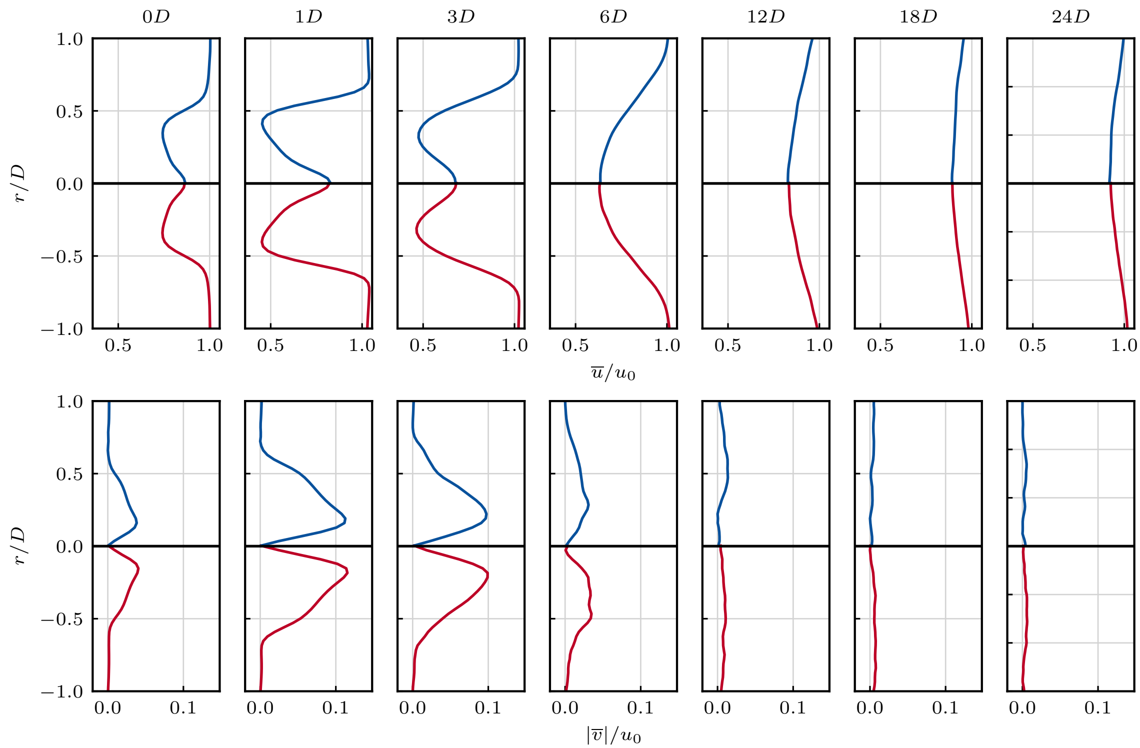

Figure 14. Cross-stream profiles of the mean stream-wise velocity $\overline{u}$ (top) and tangential velocity $\overline{v}$ (bottom) of the CLBM and NS reference in turbulent inflow. For legend, see Fig. 12.

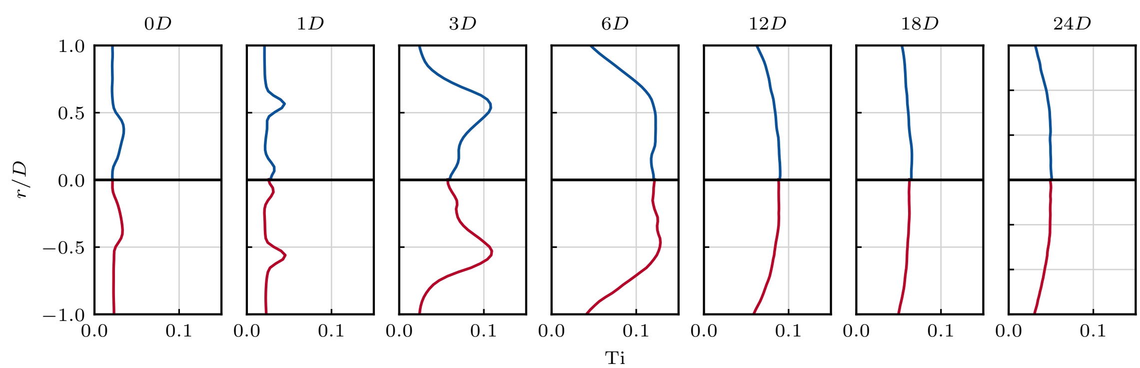

Figure 15. Cross-stream profiles of the turbulence intensity Ti of the CLBM and NS reference in turbulent inflow. For legend, see Fig. 12.

dissipation. In contrast, the imposed turbulence states a finite-size perturbation that affects the wake immediately from the rotor plane downstream independent of the numerical scheme and its dissipative properties. Similar observations in turbulent inflow have been discussed by Martínez-Tossas et al. (2018). Among others, the study assessed the impact of the ~~turbulence model in turbulent inflow was usually found to be negligible. Here, the ambient turbulence usually states the dominant factor causing the instability of the wake.~~Smagorinsky parameter C_s on wake flows in laminar and turbulent inflow. Altering C_s effectively also results in different overall diffusivities.

~~With the~~ The spectra of the turbulent kinetic energy at three different downstream positions are provided in Fig. 16. As in the laminar case, a distinct peak at the blade-passing frequency f_B and its higher harmonics can be observed in both approaches in the near-wake ($x = 1\,D$). From the velocity profiles in Fig. 14 it can be inferred that the transition of the wake occurs between $x = 3\,D$ and $x = 6\,D$, characterised by the change from a typical near-wake to a far-wake Gaussian profile. In the spectra this is reflected by an overall increase in the energy level across all resolved frequencies. Also, the signature of f_B is no longer visible. Moving further downstream ($x = 18\,D$) the overall turbulent kinetic energy decreases due to the continuous decay of both ambient and far-wake turbulence. When compared to the previous position the energy content at smaller scales increases slightly relative to the larger scales. The latter relates to the continuous break-down of the turbulent structures of the wake along the energy cascade. The relative energy increase at higher frequencies appears to be more pronounced in the CLBM solution.

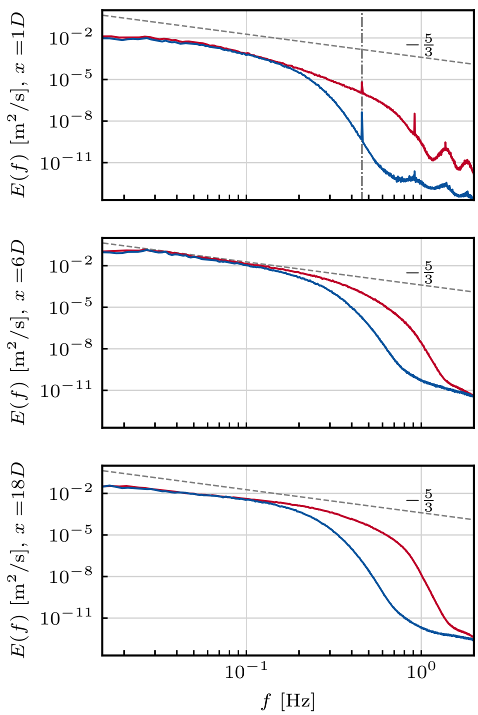

Figure 16. One-point turbulent kinetic energy spectra in the near-wake ($x = 1\,D$, top), transition-region ($x = 6\,D$, middle) and far-wake ($x = 18\,D$, bottom) in turbulent inflow. Vertical dashed-dotted line marking the blade-passing frequency f_B. For legend, see Fig. 12.

Again, this might relate to the higher dissipation found in the NS solver inducing an earlier cut-off in the sub-inertial range as discussed earlier.

Lastly, we shall comment on the small differences in the ambient turbulence shown earlier. Based on the above elaborations one might expect a more notable impact on the wake characteristics. With regards to this we refer to the study by Sørensen et al. (2015) . Based on a more extensive investigation of the impact of ambient turbulence on the length of the near-wake the authors present an empirical description of the problem. In summary, they find that the distance of the transition point to the turbine l is a function of $\ln(\mathrm{Ti})$. Following this the relative difference in l can thus be expected to be $\mathcal{O}(1-\ln(\mathrm{Ti}_{\mathrm{NS}})/\ln(\mathrm{Ti}_{\mathrm{CLBM}})) = \mathcal{O}(10^{-3})$ with the given inflows, lying well within the range of the differences observed here.

6 Impact of the Third-order Cumulant Limiter

A further aspect of the CLBM to be discussed is the impact of the limiter of the third-order cumulants described in Eq. (15)~~,~~ ~~the CLBM allows for an implicit~~ . The main motivation behind the limiter is to provide a damping of high-wave number perturbations ~~alternatively to classical turbulence models~~in the CLBM in order to ensure numerical stability. Geier et al. (2017b) showed theoretically and by means of a decaying shear-wave and Taylor-Green vortex that the use of the limiter does not affect the asymptotic order of accuracy of the scheme. Investigations of the effects of the limiter in more applied high-Reynolds-number cases are, however, not available to date. Geier et al. (2017a) and Lenz et al. (2019) presented applications of the parametrised CLBM, yet both did not touch upon the topic discussed here. Then again Pasquali et al. (2017) state that they chose suitable values for λ_m manually, close to the stability limit and case-dependent. Both the effect of λ_m on turbulent flows, as well as criteria to choose adequate values thus remain open questions. At the same time, some authors refer to the parametrised CLBM and also the AllOne as implicit LES (cf. Far et al., 2017; Lenz et al., 2019; Nishimura et al., 2019) . However, the latter is solely supported by the fact that the CLBM remains numerically stable in under-resolved turbulent flows without explicit turbulence model (as opposed to many other LBM collision operators). To the authors' knowledge, a full understanding of the dissipation behaviour associated with the limiter (or the AllOne), especially in under-resolved flows, is still lacking. This again though would be clearly required to fully replace an explicit SGS-model.

In the ~~following we investigate the impact of λ_m on the~~ code-to-code comparison the limiter was practically switched off for the sake of comparison. Hence, numerical stability was also solely provided by the Smagorinsky model. Motivated by the lacking experience with the use of the limiter we provide a brief investigation of the characteristics of the wake in comparison to the case with Smagorinsky model ~~presented~~ used in Sect. 4. For the sake of brevity ~~only~~ we only discuss a resolution of $\Delta x = D/32$~~will be looked at~~. Three values of λ_m are investigated ranging from 10^0 to 10^{-2}. The former value states the ~~smallest~~ largest possible to ensure numerical stability.~~Moreover, in addition to a simple uniform inflow we perform simulations with imposed synthetic turbulence at the inlet.~~

6.1 ~~Wake Characteristics in Uniform Inflow~~

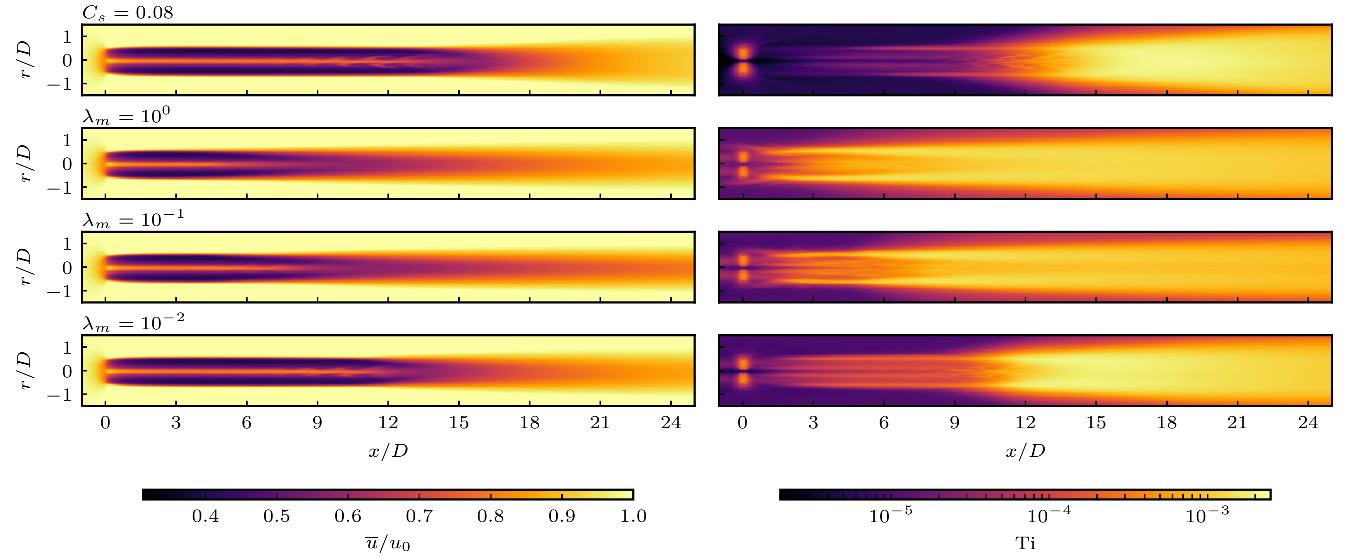

Figure 17. Contour plots of the mean stream-wise velocity $\overline{u}$ (left) and turbulence intensity Ti (right) in the central stream-wise plane in uniform inflow~~with the CLMB using the~~. Top: Smagorinsky model with pratically switched-off limiter, i.e. $\lambda_m = 10^{-6}$ (~~top~~as described in Sect. 4)~~and~~. Second to last row: no explicit turbulence model with different values of the third-order cumulant limiter~~λ_m (second to last row), repectively~~.

~~To begin with, it should be noted that the impact of the turbulence modelling on the blade loads was found to be negligible. This is in line with many of the aforementioned studies on the topic using NS formulations. A further discussion thereof is thus omitted.~~

Contour plots of the mean stream-wise velocity and turbulence intensity are shown in Fig. 17. While the mean velocity in the region close to the turbine is almost unaffected by the choice of λ_m , the evolution of the turbulence intensity and ultimately the point of transition change drastically. With $\lambda_m = 10^0$, Ti grows significantly closely behind the turbine. Only $3\,D$ downstream the wake is ~~already highly turbulent(as also shown later in ??)~~highly turbulent. With $\lambda_m = 10^{-1}$ the wake characteristics only change marginally. Increasing λ_m from 10^{-1} to 10^{-2}, however, delays the transition considerably. This implicitly shows that the order of magnitude of the third-order cumulants in crucial regions of the wake lies within this range, which can be deduced from Eq. (15). When choosing $\lambda_m = 10^{-2}$ the limiter damps the third-order cumulants considerably when compared to the optimised relaxation rates. Moreover, the far-wake distribution of Ti resembles more closely the one of the Smagorinsky case than with lower λ_m. Turbulent perturbations of the wake do, however, grow over a longer fetch than in the Smagorinsky case, starting in the near-wake. ~~Further insights can again be gained by consulting the spectra of the turbulence kinetic energy, see **??**. One-point turbulent kinetic energy spectra at different positions downstream. Vertical dashed-dotted line marking the blade-passing frequency f_B. It becomes obvious that the turbulent kinetic energy content~~

~~close to the turbine increases significantly in the near-wake ($x = 3\,D$) with increasing λ_m. Distinct peaks related to larger meandering scales are again visible. These are, however, increasingly accompanied by energies across all frequencies below f_B the higher λ_m. The pre-transition meandering, as described in Sect. 4.2, and clearly visible for the Smagorinsky case at $x = 12\,D$ is thus not as significant. The transition to a fully turbulent wake appears to occur too fast for this process to develop. A qualitative impression thereof can be obtained from the instantaneous velocity plots given in **??**. Contour plots of the instantaneous stream-wise velocity u in the central stream-wise plane. Only with $\lambda_m = 10^{-2}$ a more distinct development of such large meandering structures can again be seen, similarly to the Smagorinsky case.Lastly,~~ Moreover, it should be noted that increasing λ_m also increases the amplitude of small scale fluctuations in the ambient flow field. Among others, these are likely to be related to acoustic reflections of small scale turbulence on the domain boundaries and/or spurious numerical oscillations. Partially, these can be seen in the Ti contour plots (Fig. 17) upstream of the turbine for the two higher λ_m values. More specifically, $1\,D$ upstream of the turbine, we find $\mathrm{Ti} = \mathcal{O}(10^{-4})$ for $\lambda_m = 10^0$. In comparison, the ~~Smagorinsky case and~~ CLBM case with Smagorinsky model as well as the NS reference discussed earlier exhibit a magnitude that is two and three orders of magnitude lower, respectively. Referring to the discussions of tip-vortex stability by Ivanell et al. (2010) or Sørensen et al. (2015), an effect thereof on the break-down of the wake can not be ruled out. Unfortunately, most studies similar to the one presented here did not comment on this topic. Deskos et al. (2019), on the other hand, found that the mutual inductance of tip-vortices can be severely disturbed if the diffusivity of the scheme is too low.~~Further investigations on the effect of the limiter thus remain inevitable.~~

6.1 ~~Impact of Inflow Turbulence~~

~~Previous investigations have found that the effect of the turbulence model on the wake characteristics is almost negligible if the inflow is turbulent (Sarlak et al., 2015a; Martínez-Tossas et al., 2018). For the sake of completeness, we shall therefore perform the same parameter study with imposed synthetic turbulence at the inlet.~~

6.0.1 ~~Synthetic Turbulence Generation at the Inlet~~

~~At the inlet we prescribe homogeneous isotropic turbulence (HIT) based on the von Kármán energy spectrum. The three-dimensional field of velocity fluctuations is generated based on the method by Mann (1998) using the open-source code TuGen by Gilling (2009). As we are only interested in HIT the model's shear parameter Γ is set to zero. The length scale of the spectral velocity tensor is chosen as $L = 40\mathrm{m} = 0.317\,D$. The mean turbulence intensity is scaled via the coefficient $\alpha\epsilon^{2/3}$. The length of the turbulence field in the stream-wise direction measures 16384m. Following Taylor's frozen turbulence hypothesis the field is advected with u_0 and superimposed at the inlet. The turbulence field is consequently recycled after 4.48 domain flow-through times. The lateral dimensions of the field are set to 2048m (referring to $16.25\,D$). Since we only use a cross-section of $6\,D \times 6\,D$ we ensure zero correlation of the velocity fluctuations between the lateral boundaries of the domain. The spatial resolution of the field is 8192 grid points in the stream-wise direction and 128 grid points in the lateral directions.~~

~~In Fig. 12 we compare the stream-wise evolution of the turbulence intensity at hub-height without ALM present. Stream-wise evolution of the turbulence intensity Ti in the domain center with the CLBM without ALM. For legend, see **??**. Right behind~~

~~the inlet we observe a small increase of Ti regardless of the turbulence model. As described by Gilling and Sørensen (2011) and Keck et al. (2014) this relates to the adaptation of the velocity field to discontinuities introduced by the interpolation at the inlet. Thereafter, the turbulence continuously decays due to the absence of mean shear. For the ILES cases we find a turbulence intensity of around 8.5% at the turbine position. The turbulence intensity for the Smagorinsky cases is about 0.5% lower, which can be related to the higher dissipation introduced by~~ The presented case study underlines that the impact of the limiter is sufficiently large to arbitrarily tune the scheme's dissipativity over a wide range. Hence, the choice of the ~~model. Major differences in the spectra of the turbulence kinetic energy at hub height could not be observed, as shown in Fig. 13.~~ limiter in underresolved flows is by no means irrelevant despite the negligible influence on the asymptotic order of accuracy. On the other hand, the limiter conceivably states a measure to achieve implicit LES characteristics with the CLBM. As mentioned earlier, though, this clearly requires a more systematic understanding and subsequent tuning. Without the latter, the use of classical well-documented SGS-models might remain more practical. Ultimately, they also provide numerical stability while choices for model parameters can build on well-documented experience. ~~One-point turbulent kinetic energy spectra at the turbine position ($x = 0\,D$) with the CLBM without ALM. The spectrum of the synthetic inlet turbulence is given in grey. For legend, see **??**.~~

6.0.1 ~~Wake Characteristics~~

~~Cross-stream profiles of the mean stream-wise velocity are given in **??**. Cross-stream profiles of the stream-wise $\overline{u}$ of the CLBM with different turbulence models in turbulent inflow. For legend, see see **??**. In contrast to the results in uniform inflow, the influence of the turbulence modelling approach appears small. Generally, the break-down of the wake occurs more closely behind the turbine accompanied by a significantly faster wake recovery than in uniform inflow. Further downstream the wake quickly approaches a self-similar Gaussian profile as described by Sørensen et al. (2015). Equivalently, the turbulence intensity follows a more similar course than in uniform inflow, see **??**. The slightly smaller Ti at the turbine position in the Smagorinsky case can be seen in the wake center up until $x = 1\,D$. Further downstream the turbulence of the wake itself dominates Ti with only small differences towards the ILES cases. Cross-stream profiles of the turbulence intensity Ti of the CLBM with different turbulence models in turbulent inflow. For legend, see Fig. 5. In the turbulent cases shown here the transition of the wake is dominated by the resolved turbulent scales of the incoming flow. The dampening effect of λ_m on smaller scales thereby seems to be negligible for the general evolution of the wake. The effect of the limiter on this particular flow case is thus equally negligible as other sub-grid scales models investigated in NS frameworks (Sarlak et al., 2016; Martínez-Tossas et al., 2018).~~

7 Computational Performance

We initially outlined that the main motivation for the use of the LBM in this context is the method's superior computational performance. Nevertheless, a detailed discussion is not the focus of this paper. For further details on this topic we refer to our previous study (Asmuth et al., 2019) as well as numerous other publications, see, for instance, Schönherr et al. (2011), Obrecht et al. (2013), Januszewski and Kostur (2014), Hong et al. (2016) or Onodera et al. (2018). In brief, we shall remark that all simulations with the CLBM ran with an average of 1050 MNUPS (Million Node Updates Per Second). A similar single-GPU performance on uniform grids was recently reported by Lenz et al. (2019). For the cases discussed in this study this refers to a wall time of 524s per domain flow-through time on a single Nvidia RTX 2080 Ti on a local workstation. Putting this into perspective, the wall time per flow-through time of the NS case amounts to 5028s. The latter ran on 1044 CPU cores (Intel Xeon Gold 6130) and thus refers to 1463 CPUh. A last interesting aspect to remark is the ratio of simulated real time to computation time $r_{r2c} = \Delta t_{real}/\Delta t_{comp}$. The topic was recently addressed in the context of urban flows (Onodera and Idomura, 2018; Lenz et al., 2019) as well as for atmospheric boundary layer flows and wind energy applications (Bauweraerts and Meyers, 2019). A ratio of $r_{r2c} > 1$ would enable the use of LES for real-time forecasts of, e.g., urban micro-climates or wind farm performance and loads. For this specific LBM case we obtain $r_{r2c} = 0.902$. For the NS approach we get $r_{r2c} = 0.094$. Despite this obviously only being a case study, real-time LES of wind farms with affordable hardware demand appear possible.

8 Conclusions

The cumulant lattice Boltzmann method was applied to simulate the wake of a single wind turbine in both laminar and turbulent inflow. The turbine was represented by the actuator line model. ~~First, the~~ The presented model was compared against a well-established finite volume Navier-Stokes solver. It was shown that the cumulant lattice Boltzmann implementation of the actuator line model yields comparable first- and second-order statistics of the wake. ~~The main differences were~~ More specifically, a very good agreement of the two numerical approaches was found in the near-wake in laminar inflow. Larger discrepancies occurring in the far-wake were attributed to differences in the point of transition~~depending on the~~. These in turn could be related to the different numerical diffusivities of the schemes building onto previous similar code-to-code comparisons (Sarlak, 2014; Sarlak et al., 2016; Martínez-Tossas et al., 2018). On the other hand, the comparison in turbulent inflow showed an excellent agreement of the two solutions in both near- and far-wake. Here, differences in the numerical ~~diffusivity of the scheme. Secondly, the impact of the third-order cumulant limiter was investigated in both laminar and turbulent inflow. The latter was prescribed using the method by Mann (1998). As similarly observed in explicit sub-grid scale models, the limiter affected the wake in laminar inflow significantly. Also, it was found that a limiter close to the numerical stability limit, as suggested by others (Pasquali et al., 2017), can lead to spurious oscillations in the ambient flow. Differences in turbulent inflow were then again~~ schemes were found to be ~~small.On the one hand, the study shows~~ subordinate as the wake characteristics were dominated by the imposed turbulence.

An additional case-study investigated the impact of the third-order cumulant limiter in laminar inflow. It was shown that the choice of the limiter ~~is by no means irrelevant despite the negligible influence on the asymptotic order of accuracy (Geier et al., 2017b)~~largely affects the dissipativity of scheme. Likewise, the tuneability of this dampening characteristic clearly shows the potential to be used in a more systematic way and might be exploited as an implicit LES feature. ~~This, however,~~ Yet, this requires further fundamental investigations in order to understand and calibrate it or even develop procedures to determine optimal values dynamically. ~~Moreover, the study shows that explicit sub-grid scale modelling is not necessarily required in lattice Boltzmann frameworks to capture the flow physics of wind turbine wakes, in line with previous studies using different~~

~~Navier-Stokes discretisations (Sarlak et al., 2015a; Kleusberg et al., 2017; Deskos et al., 2019)~~As of now, the use of explicit eddy-viscosity SGS-models thus appears more practical despite a small computational overhead.

As for future applications of the lattice Boltzmann method to more realistic wind-power-related flow cases, the following conclusions can be drawn. First and foremost, the presented study underlines the suitability of the cumulant lattice Boltzmann method for the simulation of highly turbulent engineering flows. The crucial advantage over other collision operators is the superior numerical stability of the method. No other collision operator initially tested in this study was found to be sufficiently robust using the given grid resolutions. The tested single- and multiple-relaxation-time models therefore do not appear suitable for LES of entire wind farms where higher spatial resolutions are not feasible and viscosities on the lattice scale consequently small. ~~In summary, the~~ The advantages of the parametrised cumulant clearly render it as a preferable collision model for wind turbine simulations and presumably other atmospheric flows. Application-oriented studies of the model are so far limited to this work and the recent study by Lenz et al. (2019). Further investigations of the model are therefore clearly required. This applies especially to ~~the modelling of~~ wall-bounded turbulent flows like atmospheric boundary layers ~~. Furthermore, the~~ that require the use of wall-models. When compared to Navier-Stokes-based LES, the experience with wall-models in the LBM in general is limited to only a handful of studies to date (Malaspinas and Sagaut, 2014; Pasquali et al., 2017; Wilhelm et al., 2018; Nishimura et al., 2019) . More specifically, simulations of wall-modelled atmospheric boundary layers employing Monin-Obukhov-type near-wall treatments have not been reported at all to the authors' knowledge. The latter ultimately remains a crucial step towards the simulation of wind farms using the LBM. Nevertheless, in summary, the presented work underlines the great potential of wind turbine simulations using the LBM. Without suffering losses in accuracy the computational cost can be significantly reduced when compared to standard NS-based approaches. ~~In line with other discussions of the LBM (Löhner, 2019), the study shows that real-time LES of wind farms are feasible.~~

Considering the reported run-times, even an overcoming of the *LES-crisis*, i.e. the inability to obtain overnight LES solutions for industrial applications (cf. Löhner, 2019), appears possible in the context of wind farm simulations.

Code and data availability. Both ELLIPSYS3D and ELBE are proprietary software and not publicly availabe. All data presented in this study can be made available upon request.

Appendix A: ~~Prestudy~~ Pre-study on the Stability of Collision Operators

Generally, the choice of collision operator and lattice should consider stability, accuracy, memory demand and performance. Based on the seminal works by Geier et al. (2015, 2017b) the CLBM can undoubtedly be considered superior in terms of the former two. Utilising a D3Q27 lattice though eventually implies an increased memory demand of about 40%. Also, the higher complexity of the CLBM eventually renders the model computionally more expensive.

As for this specific set-up, satisfactory stability could only be achieved using the CLBM despite the use of the Smagorinsky model (for the referring formulations in moment space applied to the SRT and MRT models, see Yu et al. (2005, 2006)). The

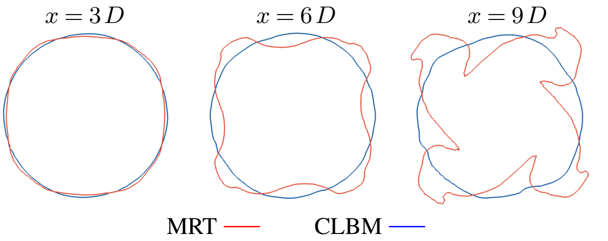

Figure A1. Instantaneous velocity contours ($u = 0.875\,u_0$) in cross-sectional planes at different positions in the wake of the turbine.

SRT generally became unstable after only a few time steps. The utilised MRT model (see, Tölke et al., 2006), on the other hand remained mostly numerically stable. Yet, unphysical oscillations in the turbulent regions of the flow led to significant degenerations throughout the entire domain.

In addition to stability issues, the isotropy of the D3Q19 lattice was shown to be insufficient. Fig. A1 shows three exemplary cross-stream velocity contours at different downstream positions. At $x = 3\,D$, small deviations from the expected axisymmetric profile can be observed for the MRT. Further downstream a more cross-like structure develops that deviates severely from an expanding circular wake. A similar behaviour on D3Q19 lattices has been described earlier by Geller et al. (2013) and Kang and Hassan (2013) when simulating circular jet and pipe flows, respectively. Both argue that the missing velocity vectors of the D3Q19 lattice cause violations of the rotional invariance of axisymmetric flows. Furthermore, White and Chong (2011) remark that this behaviour might only be obvious when simulating simple axisymmetric flows, possibly with analytical reference solutions. Nevertheless, deteriorations of non-axisymmeric real-world problems should also be anticipated, yet, might be harder to examine. This observation should thus also be taken into account when simulating wind turbines in more realistic, sheared, turbulent inflows.

Usually, stability issues as described above can be remedied by using smaller grid spacings. As we consider the latter unfeasible for the described applications, we refrain from further investigations thereof at this point. Moreover, White and Chong (2011) also show that the lacking order of isotropy of the D3Q19 lattice can only partially be reduced under grid refinement. The use of the D3Q27 lattice and the CLBM thus appears as the most suitable choice for the investigation of wind turbine wakes. Lastly, it should be pointed out that performance differences between the investigated collision operators were only found to be around 15% (all simulations ran on a single Nvidia RTX 2080 Ti in single precision).

Appendix B: ~~Local Computation of the Strain Rate Tensor in Cumulant Space~~

~~Following the asymptotic analysis of the CLBM given in Geier et al. (2015) the velocity derivatives are given as~~

$$
\begin{aligned}
\frac{\partial u}{\partial x} &= -\frac{\omega_1}{2\rho}(2C_{200} - C_{020} - C_{002}) - \frac{\omega_2}{2\rho}(2C_{200} - C_{020} + \kappa_{000}) \\
\frac{\partial v}{\partial y} &= \frac{\partial u}{\partial x} + \frac{\omega_1}{2\rho}(2C_{200} - C_{020}) \\
\frac{\partial w}{\partial z} &= \frac{\partial u}{\partial x} + \frac{\omega_1}{2\rho}(2C_{200} - C_{002}) \\
\frac{\partial v}{\partial x} + \frac{\partial u}{\partial y} &= -\frac{3\omega_1}{2\rho}C_{110} \\
\frac{\partial w}{\partial x} + \frac{\partial u}{\partial z} &= -\frac{3\omega_1}{2\rho}C_{101} \\
\frac{\partial w}{\partial y} + \frac{\partial v}{\partial z} &= -\frac{3\omega_1}{2\rho}C_{011} \quad ,
\end{aligned}
$$

~~where $C_{\alpha\beta\gamma} = \rho c_{\alpha\beta\gamma}$, with ρ being the fluid density. κ_{000} refers to the zeroth-order central velocity moment. The relaxation rate ω_1 relates to the total shear viscosity $\nu_{tot} = \nu + \nu_t$ as~~

$$\omega_1 = \left(\frac{3}{c^2}(\nu + \nu_t) + \Delta t/2\right)^{-1} \quad ,$$

~~following from Eq. (7). Due to ω_2, which is analogously linked to the bulk viscosity, **??** can not be explicitly solved for ν_t. We therefore use $\nu_t(t - \Delta t)$ for the computation of the velocity derivatives at t as outlined in Sect. 2.4.Since all cumulants as well as κ_{000} are readily available within the collision operator, the computation of $\bar{S}$ as given in the following comes at practically negligible computational cost:~~

$$\bar{S} = \left(2\left(\left(\frac{\partial u}{\partial x}\right)^2 + \left(\frac{\partial v}{\partial y}\right)^2 + \left(\frac{\partial w}{\partial z}\right)^2\right) + \left(\frac{\partial v}{\partial x} + \frac{\partial u}{\partial y}\right)^2 + \left(\frac{\partial w}{\partial x} + \frac{\partial u}{\partial z}\right)^2 + \left(\frac{\partial w}{\partial y}\right)^2 + \left(\frac{\partial v}{\partial y}\right)^2\right)^{\frac{1}{2}} \quad .$$

~~Further details on the derivation of Appendix B to **??** can be found in Geier et al. (2017b).~~

Author contributions. HA developed and implemented the LBM-ALM, performed the simulations, post-processing and data analysis and drafted the original paper. HOE and SI contributed to the conceptualisation of the study, discussion of the results and revision of the manuscript.

Competing interests. The authors declare no coflict of interest.

Acknowledgements. The authors would like to thank Martin Gehrke (TUHH) for the productive colaboration on the implementation and testing of the parametrised cumulant LBM. Also, the many fruitful discussions of the case set-up and results with Niels N. Sørensen (DTU) are highly appreciated.

EllipSys3D simulations were performed on resources provided by the Swedish National Infrastructure for Computing (SNIC) at NSC.

References

Abkar, M.: Impact of Subgrid-Scale Modeling in Actuator-Line Based Large-Eddy Simulation of Vertical-Axis Wind Turbine Wakes, Atmoshere, 9, 256, https://doi.org/doi:10.3390/atmos9070257, 2018.

Abkar, M. and Porté-Agel, F.: The Effect of Free-Atmosphere Stratification on Boundary-Layer Flow and Power Output from Very Large Wind Farms, Energies, 6, 2338–2361, https://doi.org/10.3390/en6052338, 2013.

Abkar, M., Sharifi, A., and Porté-Agel, F.: Wake flow in a wind farm during a diurnal cycle, Journal of Turbulence, 17, 420–441, https://doi.org/10.1080/14685248.2015.1127379, 2016.

Ahmad, N. H., Inagaki, A., Kanda, M., Onodera, N., and Aoki, T.: Large-Eddy Simulation of the Gust Index in an Urban Area Using the Lattice Boltzmann Method, Boundary-Layer Meteorology, 163, 447–467, https://doi.org/10.1007/s10546-017-0233-6, 2017.

Andersen, S. J., Witha, B., Breton, S.-P., Sørensen, J. N., Mikkelsen, R. F., and Ivanell, S.: Quantifying variability of Large Eddy Simulations of very large wind farms, J. Phys. Conf. Ser., 625, 012 027, https://doi.org/10.1088/1742-6596/625/1/012027, 2015.

Andre, M., Mier-Torrecilla, M., and Wüchner, R.: Numerical simulation of wind loads on a parabolic trough solar collector using lattice Boltzmann and finite element methods, J. Win. Eng. Ind. Aerod., 146, 185–194, https://doi.org/10.1016/j.jweia.2015.08.010, 2015.

Asmuth, H., Olivares-Espinosa, H., Nilsson, K., and Ivanell, S.: The Actuator Line Model in Lattice Boltzmann Frameworks: Numerical Sensitivity and Computational Performance, J. Phys. Conf. Ser., 1256, 012 022, https://doi.org/10.1088/1742-6596/1256/1/012022, 2019.

Avallone, F., van der Velden, W. C. P., Ragni, D., and Casalino, D.: Noise reduction mechanisms of sawtooth and combed-sawtooth trailing-edge serrations, J. Fluid. Mech., 848, 560–591, https://doi.org/10.1017/jfm.2018.377, 2018.

Banari, A., Gehrke, M., Janßen, C. F., and Rung, T.: Numerical simulation of nonlinear interactions in a naturally transitional flat plate boundary layer, Comput. Fluids, p. 104502, https://doi.org/https://doi.org/10.1016/j.compfluid.2020.104502, http://www.sciencedirect.com/science/article/pii/S0045793020300761, 2020.

Bauweraerts, P. and Meyers, J.: On the Feasibility of Using Large-Eddy Simulations for Real-Time Turbulent-Flow Forecasting in the Atmospheric Boundary Layer, Boundary-Layer Meteorology, 171, 213–235, https://doi.org/10.1007/s10546-019-00428-5, 2019.

Bechmann, A., Sørensen, N. N., and Zahle, F.: CFD simulations of the MEXICO rotor, Wind Energy, 14, 677–689, https://doi.org/10.1002/we.450, http://dx.doi.org/10.1002/we.450, 2011.

Bhatnagar, P., Gross, E., and Krook, M.: A Model for Collision Processes in Gases. I. Small Amplitude Processes in Charged and Neutral One-Component Systems, Phys. Rev., 94, 511–525, https://doi.org/10.1103/PhysRev.94.511, 1954.

Bouzidi, M., Firdaouss, M., and Lallemand, P.: Momentum transfer of a Boltzmann-lattice fluid with boundaries, Physics of Fluids, 13, 3452–3459, https://doi.org/http://dx.doi.org/10.1063/1.1399290, http://scitation.aip.org/content/aip/journal/pof2/13/11/10.1063/1.1399290, 2001.

Buick, J. M. and Greated, C. A.: Gravity in a lattice Boltzmann model, Phys. Rev. E, 61, 5307–5320, https://doi.org/10.1103/PhysRevE.61.5307, 2000.

Churchfield, M., Lee, S., Moriarty, P., Martinez, L., Leonardi, S., Vijayakumar, G., and Brasseur, J.: A large-eddy simulation of wind-plant aerodynamics, in: Proc. of the 50th AIAA Aerospace Sciences Meeting including the New Horizons Forum and Aerospace Exposition, p. 537, https://doi.org/10.2514/6.2012-537, 2012a.

Churchfield, M. J., Lee, S., Michalakes, J., and Moriarty, P. J.: A numerical study of the effects of atmospheric and wake turbulence on wind turbine dynamics, Journal of Turbulence, 13, N14, https://doi.org/10.1080/14685248.2012.668191, https://doi.org/10.1080/14685248.2012.668191, 2012b.

Ciri, U., Rotea, M., Santoni, C., and Leonardi, S.: Large-eddy simulations with extremum-seeking control for individual wind turbine power optimization, Wind Energy, 20, 1617–1634, https://doi.org/10.1002/we.2112, 2017.

Deiterding, R. and Wood, S. L.: Predictive wind turbine simulation with an adaptive lattice Boltzmann method for moving boundaries, J. Phys.: Conf. Series, 753, 082 005, https://doi.org/10.1088/1742-6596/753/8/082005, 2016.

Dellar, P. J.: Bulk and shear viscosities in lattice Boltzmann equations, Phys. Rev. E, 64, 031 203, https://doi.org/10.1103/PhysRevE.64.031203, 2001.

Dellar, P. J.: Incompressible limits of lattice boltzmann equations using multiple relaxation times, J. Comput. Phys, p. 2003, https://doi.org/10.1016/S0021-9991(03)00279-1, 2003.

Deskos, G., Laizet, S., and Piggott, M. D.: Turbulence-resolving simulations of wind turbine wakes, Renew. Energ., 134, 989 –1002, https://doi.org/10.1016/j.renene.2018.11.084, 2019.

d'Humières, D., Ginzburg, I., Krafczyk, M., Lallemand, P., and Luo, L.-S.: Multiple-relaxation-time lattice Boltzmann models in three dimensions, Philos. Trans. R. Soc. London, A, 360, 437–451, https://doi.org/10.1098/rsta.2001.0955, 2002.

Dilip, D. and Porté-Agel, F.: Wind Turbine Wake Mitigation through Blade Pitch Offset, Energies, 10, https://doi.org/10.3390/en10060757, 2017.

Fang, J., Peringer, A., Stupariu, M.-S., Pătru-Stupariu, I., Buttler, A., Golay, F., and Porté-Agel, F.: Shifts in wind energy potential following land-use driven vegetation dynamics in complex terrain, Sci. Tot. Environ., 639, 374–384, https://doi.org/10.1016/j.scitotenv.2018.05.083, 2018.

Far, E., Geier, M., Kutscher, K., and Krafczyk, M.: Implicit Large Eddy Simulation of Flow in a Micro-Orifice with the Cumulant Lattice Boltzmann Method, Computation, 5, 23, https://doi.org/10.3390/computation5020023, 2017.

Far, E. K., Geier, M., Kutscher, K., and Krafczyk, M.: Simulation of micro aggregate breakage in turbulent flows by the cumulant lattice Boltzmann method, Comput. Fluids, 140, 222 – 231, https://doi.org/10.1016/j.compfluid.2016.10.001, 2016.

Fleming, P., Gebraad, P. M., Lee, S., Wingerden, J., Johnson, K., Churchfield, M., Michalakes, J., Spalart, P., and Moriarty, P.: Simulation comparison of wake mitigation control strategies for a two-turbine case, Wind Energy, 18, 2135–2143, https://doi.org/10.1002/we.1810, 2015.

Foti, D. and Duraisamy, K.: Implicit Large-Eddy Simulation of Wind Turbine Wakes and Turbine-Wake Interactions using the Vorticity Transport Equations, Proc. of the AIAA Aviation 2019 Forum, https://doi.org/10.2514/6.2019-2841, 2019.

Fragner, M. and Deiterding, R.: Investigating cross-wind stability of high-speed trains with large-scale parallel CFD, Int. J. Comput. Fluid. D., 30, 402–407, https://doi.org/10.1080/10618562.2016.1205188, 2016.

Gehrke, M., Janßen, C., and Rung, T.: Scrutinizing lattice Boltzmann methods for direct numerical simulations of turbulent channel flows, Comput. Fluids, 156, 247–263, https://doi.org/10.1016/j.compfluid.2017.07.005, 2017.

Gehrke, M., Banari, A., and Rung, T.: Performance of Under-Resolved, Model-Free LBM Simulations in Turbulent Shear Flows, Notes on Numerical Fluid Mechanics and Multidisciplinary Design. Progress in Hybrid RANS-LES Modelling, 143, 3–18, https://doi.org/10.1007/978-3-030-27607-2_1, 2020.

Geier, M., Schönherr, M., Pasquali, A., and Krafczyk, M.: The cumulant lattice Boltzmann equation in three dimensions: Theory and validation, Comput. Math. Appl., 70, 507–547, https://doi.org/10.1016/j.camwa.2015.05.001, 2015.

Geier, M., Pasquali, A., and Schönherr, M.: Parametrization of the cumulant lattice Boltzmann method for fourth order accurate diffusion part II: Application to flow around a sphere at drag crisis, J. Comput. Phys., 348, 889 – 898, https://doi.org/10.1016/j.jcp.2017.07.004, 2017a.

Geier, M., Pasquali, A., and Schönherr, M.: Parametrization of the cumulant lattice Boltzmann method for fourth order accurate diffusion part I: Derivation and validation, J. Comput. Phys., 348, 862–888, https://doi.org/10.1016/j.jcp.2017.05.040, 2017b.

Geller, S., Uphoff, S., and Krafczyk, M.: Turbulent jet computations based on MRT and Cascaded Lattice Boltzmann models, Computers & Mathematics with Applications, 65, 1956 –1966, https://doi.org/10.1016/j.camwa.2013.04.013, 2013.

Gilling, L.: TuGen: Synthetic Turbulence Generator, Manual and User's Guide, Tech. Rep. 76, Department of Civil Engineering, Aalborg University, 2009.

Gilling, L. and Sørensen, N. N.: Imposing resolved turbulence in CFD simulations, Wind Energy, 14, 661–676, https://doi.org/10.1002/we.449, 2011.

Ginzburg, I. and Adler, P.: Boundary flow condition analysis for the three-dimensional lattice Boltzmann model, J. Phys. II France, 4, 191–214, https://doi.org/10.1051/jp2:1994123, 1994.

Ginzburg, I., Verhaeghe, F., and d'Humières, D.: Two-Relaxation-Time Lattice Boltzmann Scheme: About Parametrization, Velocity, Pressure and Mixed Boundary Conditions, Commun. Comput. Phys., 3, 427–478, 2008.

Guo, Z., Zheng, C., and Shi, B.: Lattice Boltzmann equation with multiple effective relaxation times for gaseous microscale flow, Phys. Rev. E, 77, 036 707, https://doi.org/10.1103/PhysRevE.77.036707, 2008.

Hansen, M. O.: Aerodynamics of Wind Turbines, London, UK: Earthscan, 2008.

He, X. and Luo, L.-S.: Lattice Boltzmann Model for the Incompressible Navier–Stokes Equation, J. Stat. Phys., 88, 927–944, https://doi.org/10.1023/B:JOSS.0000015179.12689.e4, 1997.

Hong, P.-Y., Huang, L.-M., Lin, L.-S., and Lin, C.-A.: Scalable multi-relaxation-time lattice Boltzmann simulations on multi-GPU cluster, Computers & Fluids, 110, 1–8, https://doi.org/10.1016/j.compfluid.2014.12.010, 2016.

Hou, S., Sterling, J., Chen, S., and Doolen, D.: A Lattice Boltzmann Subgrid Model for High Reynolds Number Flows, in: Pattern Formation and Lattice Gas Automata, Fields Institute Com- munications, vol. 6, https://doi.org/arXiv:comp-gas/9401004, 1996.

Ivanell, S., Mikkelsen, R., Sørensen, J. N., and Henningson, D.: Stability Analysis of the Tip Vortices of a Wind Turbine, Wind Energy, 13, 705–715, https://doi.org/10.1002/we.391, 2010.

Ivanell, S., Arnqvist, J., Avila, M., Cavar, D., Chavez-Arroyo, R. A., Olivares-Espinosa, H., Peralta, C., Adib, J., and Witha, B.: Microscale model comparison (benchmark) at the moderate complex forested site Ryningsnäs, Wind Energ. Sci. Discussions, 2018, 1–27, https://doi.org/10.5194/wes-2018-20, 2018.

Jacob, J. and Sagaut, P.: Wind comfort assessment by means of large eddy simulation with lattice Boltzmann method in full scale city area, Build. Environ., 139, 110 – 124, https://doi.org/10.1016/j.buildenv.2018.05.015, 2018.

Jafari, S. and Mohammad, R.: Shear-improved Smagorinsky modeling of turbulent channel flow using generalized Lattice Boltzmann equation, International Journal for Numerical Methods in Fluids, 67, 700–712, https://doi.org/10.1002/fld.2384, 2011.

Janßen, C. F., Mierke, D., Überrück, M., Gralher, S., and Rung, T.: Validation of the GPU-Accelerated CFD Solver ELBE for Free Surface Flow Problems in Civil and Environmental Engineering, Computation, 3, 354, https://doi.org/10.3390/computation3030354, 2015.

Janßen, C. F., Mierke, D., and Rung, T.: On the development of an efficient numerical ice tank for the simulation of fluid-ship-rigid-ice interactions on graphics processing units, Computers & Fluids, 155, 22 – 32, https://doi.org/10.1016/j.compfluid.2017.05.006, iCMMES2015, 2017.

Januszewski, M. and Kostur, M.: Sailfish: A flexible multi-GPU implementation of the lattice Boltzmann method, Computer Physics Communications, 185, 2350 – 2368, https://doi.org/10.1016/j.cpc.2014.04.018, 2014.

Jha, P. K., Churchfield, M. J., Moriarty, P. J., and Schmitz, S.: Guidelines for Volume Force Distributions Within Actuator Line Modeling of Wind Turbines on Large-Eddy Simulation-Type Grids, J. Sol. Energy Eng., 136, 2013.

Jonkman, J., Butterfield, S., Musial, W., and Scott, G.: Definition of a 5-MW Reference Wind Turbine for Offshore System Development, Tech. Rep. NREL/TP-500-38060, NREL, 2009.

Kang, S. K. and Hassan, Y. A.: The effect of lattice models within the lattice Boltzmann method in the simulation of wall-bounded turbulent flows, J. Comput. Phys., 232, 100 – 117, https://doi.org/10.1016/j.jcp.2012.07.023, 2013.

Keck, R.-E., Mikkelsen, R., Troldborg, N., de Maré, M., and Hansen, K. S.: Synthetic atmospheric turbulence and wind shear in large eddy simulations of wind turbine wakes, Wind Energy, 17, 1247–1267, https://doi.org/10.1002/we.1631, https://onlinelibrary.wiley.com/doi/abs/10.1002/we.1631, 2014.

Khan, A.: Finite element analysis of aerodynamic coefficients of a HAWT blade using LBM method, AIP Conference Proc., 1980, 040 007, https://doi.org/10.1063/1.5044317, 2018.

King, M.-F., Khan, A., Delbosc, N., Gough, H. L., Halios, C., Barlow, J. F., and Noakes, C. J.: Modelling urban airflow and natural ventilation using a GPU-based lattice-Boltzmann method, Build. Environ., 125, 273 – 284, https://doi.org/10.1016/j.buildenv.2017.08.048, 2017.

Kleusberg, E., Mikkelsen, R. F., Schlatter, P., Ivanell, S., and Henningson, D. S.: High-Order Numerical Simulations of Wind Turbine Wakes, J. Phys.: Conf. Series, 854, 012 025, https://doi.org/10.1088/1742-6596/854/1/012025, 2017.

Krafczyk, M., Tölke, J., and Luo, L.-S.: Large-eddy simulations with a multiple-relaxation-time LBE model, Int. J. Mod. Phys. B, 17, 33–39, https://doi.org/10.1142/S0217979203017059, 2003.

Krüger, T., Kusumaatmaja, H., Kuzmin, A., Shardt, O., Silva, G., and Viggen, E. M.: The Lattice Boltzmann Method - Principles and Practice, Heidelberg, Germany: Springer, 2016.

Kutscher, K., Geier, M., and Krafczyk, M.: Multiscale simulation of turbulent flow interacting with porous media based on a massively parallel implementation of the cumulant lattice Boltzmann method, Comput. Fluids, In Press, https://doi.org/10.1016/j.compfluid.2018.02.009, 2018.

Lallemand, P. and Luo, L.-S.: Theory of the lattice Boltzmann method: Dispersion, dissipation, isotropy, Galilean invariance, and stability, Phys. Rev. E, 61, 6546–6562, https://doi.org/10.1103/PhysRevE.61.6546, 2000.

Lallemand, P. and Luo, L.-S.: Lattice Boltzmann method for moving boundaries, J. Comput. Phys., 184, 406–421, https://doi.org/http://dx.doi.org/10.1016/S0021-9991(02)00022-0, 2003.

Lenz, S., Schönherr, M., Geier, M., Krafczyk, M., Pasquali, A., Christen, A., and Giometto, M.: Towards real-time simulation of turbulent air flow over a resolved urban canopy using the cumulant lattice Boltzmann method on a GPGPU, J. Win. Eng. Ind. Aerod., 189, 151 – 162, https://doi.org/10.1016/j.jweia.2019.03.012, 2019.

Löhner, R.: Towards overcoming the LES crisis, Int. J. Comput. Fluid. D., 33, 87–97, https://doi.org/10.1080/10618562.2019.1612052, 2019.

Malaspinas, O. and Sagaut, P.: Advanced large-eddy simulation for lattice Boltzmann methods: The approximate deconvolution model, Physics of Fluids, 23, 105 103, https://doi.org/10.1063/1.3650422, 2011.

Malaspinas, O. and Sagaut, P.: Wall model for large-eddy simulation based on the lattice Boltzmann method, J. Comput. Phys., 275, 25 – 40, https://doi.org/10.1016/j.jcp.2014.06.020, 2014.

Mann, J.: Wind field simulation, Probabilist. Eng. Mech., 13, 269 – 282, https://doi.org/10.1016/S0266-8920(97)00036-2, 1998.

Martínez-Tossas, L. A. and Meneveau, C.: Filtered lifting line theory and application to the actuator line model, J. Fluid Mech., 863, 269–292, https://doi.org/10.1017/jfm.2018.994, 2019.

Martínez-Tossas, L. A., Churchfield, M. J., and Leonardi, S.: Large eddy simulations of the flow past wind turbines: actuator line and disk modeling, Wind Energy, 18, 1047–1060, https://doi.org/10.1002/we.1747, 2015.

Martínez-Tossas, L. A., Churchfield, M. J., Yilmaz, A. E., Sarlak, H., Johnson, P. L., Sørensen, J. N., Meyers, J., and Meneveau, C.: Comparison of four large-eddy simulation research codes and effects of model coefficient and inflow turbulence in actuator-line-based wind turbine modeling, J. Renewable Sustainable Energy, 10, 033 301, https://doi.org/10.1063/1.5004710, 2018.

Mehta, D., van Zuijlen, A., Koren, B., Holierhoek, J., and Bijl, H.: Large Eddy Simulation of wind farm aerodynamics: A review, J. Wind Eng. Ind. Aerodyn., 133, 1 – 17, https://doi.org/10.1016/j.jweia.2014.07.002, 2014.

Meng, H., Lien, F.-S., and Li, L.: Elastic actuator line modelling for wake-induced fatigue analysis of horizontal axis wind turbine blade, Renew. Energ., 116, 423 – 437, https://doi.org/10.1016/j.renene.2017.08.074, 2018.

Merlier, L., Jacob, J., and Sagaut, P.: Lattice-Boltzmann Large-Eddy Simulation of pollutant dispersion in street canyons including tree planting effects, Atmospheric Environment, 195, 89–103, https://doi.org/10.1016/j.atmosenv.2018.09.040, 2018.

Merlier, L., Jacob, J., and Sagaut, P.: Lattice-Boltzmann large-eddy simulation of pollutant dispersion in complex urban environment with dense gas effect: Model evaluation and flow analysis, Building and Environment, 148, 634–652, https://doi.org/10.1016/j.buildenv.2018.11.009, 2019.

Meyer Forsting, A. R., Pirrung, G. R., and Ramos-García, N.: A vortex-based tip/smearing correction for the actuator line, Wind Energ. Sci., 4, 369–383, https://doi.org/10.5194/wes-4-369-2019, 2019.

Michelsen, J. A.: Basis3D—A platform for development of multiblock PDE solvers, Tech. Rep. Report AFM 92-05, Technical University of Denmark, DTU, 1994a.

Michelsen, J. A.: Block structured multigrid solution of 2D and 3D elliptic PDE's, Tech. Rep. Report AFM 94-06, Technical University of Denmark, DTU, 1994b.

Mierke, D., Janßen, C., and Rung, T.: An efficient algorithm for the calculation of sub-grid distances for higher-order LBM boundary conditions in a GPU simulation environment, Comput. Math. Appl., https://doi.org/10.1016/j.camwa.2018.04.022, 2018.

Mohebbi, M. and Rezvani, M. A.: Multi objective optimization of aerodynamic design of high speed railway windbreaks using Lattice Boltzmann Method and wind tunnel test results, International Journal of Rail Transportation, 6, 183–201, https://doi.org/10.1080/23248378.2018.1463873, 2018.

Munters, W. and Meyers, J.: Dynamic Strategies for Yaw and Induction Control of Wind Farms Based on Large-Eddy Simulation and Optimization, Energies, 11, https://doi.org/10.3390/en11010177, 2018.

Nathan, J., Masson, C., and Dufresne, L.: Near-wake analysis of actuator line method immersed in turbulent flow using large-eddy simulations, Wind Energy Science, 3, 905–917, https://doi.org/10.5194/wes-3-905-2018, 2018.

Nathen, P., Haussmann, M., Krause, M., and Adams, N.: Adaptive filtering for the simulation of turbulent flows with lattice Boltzmann methods, Computers & Fluids, 172, 510 – 523, https://doi.org/10.1016/j.compfluid.2018.03.042, 2018.

Nebenführ, B. and Davidson, L.: Prediction of wind-turbine fatigue loads in forest regions based on turbulent LES inflow fields, Wind Energy, 20, 1003–1015, https://doi.org/10.1002/we.2076, 2017.

Nilsson, K., Ivanell, S., Hansen, K. S., Mikkelsen, R., Sørensen, J. N., Breton, S.-P., and Henningson, D.: Large eddy simulations of the Lillegrund wind farm, Wind Energy, 18, 449–467, https://doi.org/10.1002/we.1707, 2015.

Nishimura, S., Hayashi, K., Nakaye, S., Yoshimoto, M., Suga, K., and Inamuro, T.: Implicit Large-Eddy Simulation of rotating and non-rotating machinery with Cumulant Lattice Boltzmann method aiming for industrial applications, Proc. AIAA Aviation 2019 Forum, https://doi.org/10.2514/6.2019-3526, 2019.

Obrecht, C., Kuznik, F., Tourancheau, B., and Roux, J.-J.: Multi-GPU implementation of the lattice Boltzmann method, Comput. Math. Appl., 65, 252 – 261, https://doi.org/10.1016/j.camwa.2011.02.020, 2013.

Olivares-Espinosa, H., Breton, S.-P., Nilsson, K., Masson, C., Dufresne, L., and Ivanell, S.: Assessment of Turbulence Modelling in the Wake of an Actuator Disk with a Decaying Turbulence Inflow, Applied Sciences, 8, https://doi.org/10.3390/app8091530, 2018.

Onodera, N. and Idomura, Y.: Acceleration of Wind Simulation Using Locally Mesh-Refined Lattice Boltzmann Method on GPU-Rich Supercomputers, in: Supercomputing Frontiers, edited by Yokota, R. and Wu, W., pp. 128–145, Springer International Publishing, 2018.

Onodera, N., Idomura, Y., Ali, Y., and Shimokawabe, T.: Communication Reduced Multi-time-step Algorithm for Real-time Wind Simulation on GPU-based Supercomputers, Proc. of the The International Conference for High Performance Computing, Networking, Storage, and Analysis, Dallas, USA, https://doi.org/10.1109/ScalA.2018.00005, 2018.

Pasquali, A., Geier, M., and Krafczyk, M.: Near-wall treatment for the simulation of turbulent flow by the cumulant lattice Boltzmann method, Comput. Math. Appl., 79, 195–212, https://doi.org/10.1016/j.camwa.2017.11.022, 2017.

Porté-Agel, F., Wu, Y.-T., Lu, H., and Conzemius, R. J.: Large-eddy simulation of atmospheric boundary layer flow through wind turbines and wind farms, J. Win. Eng. Ind. Aerod., 99, 154 – 168, https://doi.org/https://doi.org/10.1016/j.jweia.2011.01.011, http://www.sciencedirect.com/science/article/pii/S0167610511000134, 2011.

Premnath, K. N., Pattison, M. J., and Banerjee, S.: Generalized lattice Boltzmann equation with forcing term for computation of wall-bounded turbulent flows, Phys. Rev. E, 79, 026 703, https://doi.org/10.1103/PhysRevE.79.026703, 2009a.

Premnath, K. N., Pattison, M. J., and Banerjee, S.: Dynamic subgrid scale modeling of turbulent flows using lattice-Boltzmann method, Physica A, 388, 2640–2658, https://doi.org/10.1016/j.physa.2009.02.041, 2009b.

Qian, Y.-H., D'Humières, D., and Lallemand, P.: Lattice BGK models for Navier-Stokes equation, Europhysics Letters, 17, 479, https://doi.org/10.1209/0295-5075/17/6/001, 1992.

Roache, P.: Verification of Codes and Calculations, AIAA Journal, 36, 696–702, 1998.

Rullaud, S., Blondel, F., and Cathelain, M.: Actuator-Line Model in a Lattice Boltzmann Framework for Wind Turbine Simulations, J. Phys.: Conf. Series, 1037, 022 023, https://doi.org/10.1088/1742-6596/1037/2/022023, 2018.

Sagaut, P.: Toward advanced subgrid models for Lattice-Boltzmann-based Large-eddy simulation: Theoretical formulations, Comput. Math. Appl., 59, 2194–2199, https://doi.org/10.1016/j.camwa.2009.08.051, 2010.

Sanderse, B., van der Pijl, S., and Koren, B.: Review of computational fluid dynamics for wind turbine wake aerodynamics, Wind Energy, 14, 799–819, https://doi.org/10.1002/we.458, 2011.

Sarlak, H.: Large Eddy Simulation of Turbulent Flows in Wind Energy, Ph.D. thesis, DTU Wind Energy, Denmark, 2014.

Sarlak, H., Meneveau, C., and Sørensen, J.: Role of subgrid-scale modeling in large eddy simulation of wind turbine wake interactions, Renew. Energ., 77, 386–399, https://doi.org/10.1016/j.renene.2014.12.036, 2015a.

Sarlak, H., Meneveau, C., Sørensen, J. N., and Mikkelsen, R.: Quantifying the Impact of Subgrid Scale Models in Actuator-Line Based LES of Wind Turbine Wakes in Laminar and Turbulent Inflow, in: Direct and Large-Eddy Simulation IX, edited by Fröhlich, J., Kuerten, H., Geurts, B. J., and Armenio, V., pp. 169–175, Springer International Publishing, Cham, 2015b.

Sarlak, H., Nishino, T., Martínez-Tossas, L., Meneveau, C., and Sørensen, J.: Assessment of blockage effects on the wake characteristics and power of wind turbines, Renew. Energ., 93, 340 – 352, https://doi.org/10.1016/j.renene.2016.01.101, 2016.

Sarmast, S., Dadfar, R., Mikkelsen, R. F., Schlatter, P., Ivanell, S., Sørensen, J. N., and Henningson, D. S.: Mutual inductance instability of the tip vortices behind a wind turbine, J. Fluid. Mech., 755, 705–731, https://doi.org/10.1017/jfm.2014.326, 2014.

Schönherr, M., Kucher, K., Geier, M., Stiebler, M., Freudiger, S., and Krafczyk, M.: Multi-thread implementations of the lattice Boltzmann method on non-uniform grids for CPUs and GPUs, Comput. Math. Appl., 61, https://doi.org/10.1016/j.camwa.2011.04.012, 2011.

Sørensen, J. N. and Shen, W. Z.: Numerical Modeling of Wind Turbine Wakes, J. Fluids Eng., 124, 393–399, https://doi.org/10.1115/1.1471361, 2002.

Sørensen, J. N., Mikkelsen, R. F., Henningson, D. S., Ivanell, S., Sarmast, S., and Andersen, S. J.: Simulation of wind turbine wakes using the actuator line technique, Philosophical Transactions of the Royal Society of London A: Mathematical, Physical and Engineering Sciences, 373, 2015.

Sørensen, N. N.: General purpose flow solver applied to flow over hills, Ph.D. thesis, Risø National Laboratory, Roskilde, Denmark, 1995.

Storey, R., Cater, J., and Norris, S.: Large eddy simulation of turbine loading and performance in a wind farm, Renew. Energ., 95, 31 – 42, https://doi.org/10.1016/j.renene.2016.03.067, 2016.

Succi, S.: Lattice Boltzmann 2038, Europhysics Letters, 109, 50 001, https://doi.org/10.1209/0295-5075/109/50001, 2015.

Tölke, S., Freudiger, S., and Krafczyk, M.: An adaptive scheme using hierarchical grids for lattice Boltzmann multi-phase flow simulations, Computers & Fluids, 35, 820–830, https://doi.org/10.1016/j.compfluid.2005.08.010, 2006.

Troldborg, N.: Actuator Line Modeling of Wind Turbine Wakes, Ph.D. thesis, Technical University of Denmark, Department of Mechanical Engineering, 2008.

Troldborg, N., Sørensen, J. N., and Mikkelsen, R.: Numerical simulations of wake characteristics of a wind turbine in uniform inflow, Wind Energy, 13, 86–99, https://doi.org/10.1002/we.345, 2010.

van der Laan, M. P., Andersen, S. J., Ramos García, N., Angelou, N., Pirrung, G. R., Ott, S., Sjöholm, M., Sørensen, K. H., Vianna Neto, J. X., Kelly, M., Mikkelsen, T. K., and Larsen, G. C.: Power curve and wake analyses of the Vestas multi-rotor demonstrator, Wind Energ. Sci., 4, 251–271, https://doi.org/10.5194/wes-4-251-2019, 2019.

van der Velden, W., Pröbsting, S., van Zuijlen, A., de Jong, A., Guan, Y., and Morris, S.: Numerical and experimental investigation of a beveled trailing-edge flow field and noise emission, Journal of Sound and Vibration, 384, 113–129, https://doi.org/10.1016/j.jsv.2016.08.005, 2016.

Weickert, M., Teike, G., Schmidt, O., and Sommerfeld, M.: Investigation of the LES WALE turbulence model within the lattice Boltzmann framework, Comput. Math. Appl., 59, 2200–2214, https://doi.org/10.1016/j.camwa.2009.08.060, 2010.

White, A. T. and Chong, C. K.: Rotational invariance in the three-dimensional lattice Boltzmann method is dependent on the choice of lattice, J. Comput. Phys., 230, 6367 – 6378, https://doi.org/10.1016/j.jcp.2011.04.031, 2011.

Wilhelm, S., Jacob, J., and Sagaut, P.: An explicit power-law-based wall model for lattice Boltzmann method–Reynolds-averaged numerical simulations of the flow around airfoils, Physics of Fluids, 30, 065 111, https://doi.org/10.1063/1.5031764, https://doi.org/10.1063/1.5031764, 2018.

Yu, H., Girimaji, S. S., and Luo, L.-S.: DNS and LES of decaying isotropic turbulence with and without frame rotation using lattice Boltzmann method, J. Comput. Phys., 209, 599 – 616, https://doi.org/10.1016/j.jcp.2005.03.022, 2005.

Yu, H., Luo, L.-S., and Girimaji, S. S.: LES of turbulent square jet flow using an MRT lattice Boltzmann model, Computers & Fluids, 35, 957–965, https://doi.org/10.1016/j.compfluid.2005.04.009, 2006.

Zhiqiang, L., Yunke, W., Jie, H., Zhihong, Z., and Wenqi, C.: The study on performance and aerodynamics of micro counter-rotating HAWT, Energy, 161, 939–954, https://doi.org/10.1016/j.energy.2018.07.049, 2018.